Analysis of performance and flow structures of cycloidal rotors under different pitch-pivot-point and blade camber conditions

Lei Shi, Desheng Zhang, Annie-Claude Bayeul-Lainé, Olivier Coutier-Delgosha

Analysis of performance and flow structures of cycloidal rotors under different pitch-pivot-point and blade camber conditions

Lei Shi[1,2,a], Desheng Zhang[1], Annie-Claude Bayeul-Laine[2], Olivier Coutier-Delgosha[2,3]

[1]*Research Center of Fluid Machinery Engineering and Technology, Jiangsu University, Zhenjiang 212013, China*

[2]*Arts et Métiers ParisTech, ONERA, CNRS, Univ. Lille, Centrale Lille, UMR 9014-LMFL-Laboratoire de Mécanique des Fluides de Lille-Kampé de Fériet, F-59000 Lille, France*

[3]*Kevin T. Crofton Department of Aerospace and Ocean Engineering, Virginia Tech, Blacksburg, VA 24060, USA*

[a]Corresponding author e-mail: mumuyedda@126.com

Abstract

The performance and unsteady vortical flows of a 2-bladed cycloidal propeller are investigated using the SST $\gamma - \overline{Re}_{\theta t}$ transition model, under different pitch-pivot-point and blade camber conditions. Firstly, it shows that the results of the present computations match well with the previous numerical data and experiments, in terms of the instantaneous performance and internal flow structures. Then, due to the moderate propulsive force and low power, the cycloidal rotor with a pitch-pivot-point of x/c=0.25 maximize the efficiency. Moving the pitching location to the leading edge increases the lift and leads to the earlier flow separation on the blade surface. However, as the pitch-pivot-point shifts to the middle chord, the power of the cycloidal rotor increases dramatically because of the massive flow separation, leading to the degradation of the performance. Simultaneously, the symmetrical profiles, involving NACA0012 and 0015, are recommended due to the wide operation condition with high efficiency. The thick symmetrical and asymmetrical airfoils produce the worst performance due to the large power that is consumed. Furthermore, owing to the change of the rotating speed only, the advance coefficient effect is more obvious than the Reynolds number. When analyzing the performance of the rotating system at any position, one should consider the performance, pressure difference, near-wall flows and forces (lift and drag) of each blade.

Keywords: Cycloidal propeller; Pitch-pivot-point; Blade profile; Advance coefficient

1. Introduction

As a new kind of vertical-axis propulsive devices, cycloidal propellers comprising several vertical blades, are widely used to many engineering applications, such as the unmanned aerial vehicle and underwater propulsion system. The operation principle of the cycloidal propeller includes the rotation around the shaft center and the pitching motion based on a pivot point along the blade chord. In a revolution, the vortical flow inside the cycloidal rotor is extremely complex, characterized by the blade-wake and wake-wake interactions [1]. The performance of the single blade and cycloidal propeller depends on many parameters, such as the advance coefficient, Reynolds number, chord-to-radius ratio, blade camber, solidity and pitch-pivot-point. As a consequence, with the goal of improving the performance of the cycloidal propeller, the first step is to investigate the influence of these parameters mentioned above.

The pitch-pivot-point is found to affect the propulsive force and wake flow of pitching airfoils significantly, and moving it forward or backward is equal to add a plunging motion to the original pitching motion [2]. In most cases, the pitch-pivot-point at x/c=0.25 can optimize the performance of oscillating airfoils or vertical-axis turbines. However, Xisto et al. [3] reported that for a given pitching amplitude, the optimum location depends on the tip speed ratio (TSR), but should be located in the range $0.35<x/c<0.50$. In cycloidal rotor, Benedict et al. [4] conducted the experiments to investigate two important parameters, namely the chord-to-radius ratio and pitching axis location, and the results show that moving the pitch-pivot-point closer to the leading edge increases the lift producing efficiency of the cyclorotor. Then, Benedict et al. [5] observed that shifting the pitching axis location from the leading edge can improve the performance, with the optimum pitching axis location being 25%-35% chord. Until now, there is a debate about the optimal pitch-pivot-point, and how the near-wall flow influences the performance at different pitching point conditions are still unclear.

Blade profile is of great importance to the performance of the cycloidal propeller due to the geometry curvature that can change the internal flow structure. Most often, the symmetrical airfoils are selected. However, the reason why symmetrical airfoils are adopted and asymmetrical profiles are not feasible are not understood well. For the moment, some progress has been made about the geometry effect. Jarugumilli et al. [6] investigated three symmetrical airfoils with application to a micro-air-vehicle (MAV) scale cycloidal rotor, and the conclusion is that the thicker airfoil has the highest power loading (thrust/power), due to the higher leading-edge suction and the better stall property. Zhang et al. [7] tested a quantity of symmetrical and asymmetrical airfoil cambers when the cycloidal propeller is under hover status, and stated that based on the figure of merit (FM, the ratio of the ideal

power to the actual power required to the hover), NACA8515 airfoil has the lowest FM, while NACA0015 and inverse NACA2515 airfoils have the highest FM. Moreover, Tang et al. [8] adopted a new aerodynamic-optimization-design method to have a better design of an airfoil, and found that the optimized airfoil has a higher maximal thickness than the baseline NACA0015. Simultaneously, a suggestion that an airfoil with a suitable amount of positive camber is possibly a better choice than the symmetrical airfoil for cycloidal propellers is proposed. In vertical-axis turbines or propellers, the three-dimensional blade can be designed with different shapes to improve the performance, such as the bionic blade [9-10], trapped vortex cavity blade [11], the slotted blade [12] and blade with bio-inspired leading-edge tubercles [13].

Inspired by the aforementioned study, the goal of the present work is to investigate the influence of the pitch-pivot-point and blade camber on the performance and flow structures of 2-bladed cycloidal propeller using the computations. Then, for a specific blade profile, the advance coefficient effect is considered. The main focus is on how the near-wall flow affects the performance of the single blade and the rotating system under various conditions.

2. Problem description

2.1 Geometrical parameters and computational configuration

As shown in figure 1a, the 2-bladed cycloidal rotor with NACA0015 airfoil is employed. It rotates in the clockwise direction with different rotating speed. The lift force of the rotating system is provided by the vertical force components of two blades while the horizontal force components are responsible for the propulsive force. In the previous work [14], it is found that the chord-to-radius ratio c/R=0.45 (R is the distance between the origin of the coordinate and the blade pitch-pivot-point) can maximize the propulsive force and efficiency, which has a little bit increase with the chord length. In addition, it is also observed that an asymmetrical pitching kinematic, involving a mean pitch angle of 5° and a pitching amplitude of 35°, achieves the best performance of the rotating system. The instantaneous pitch angle θ refers to the angle between the blade chord line and the tangential direction of the rotating trajectory [15], and it varies continusously in a revolution, which is plotted in figure 1b. The main geometrical parameters are listed in table 1. It should be noted that the definition of the power coefficient is associated with the spanwise length H. In two-dimensional flow, H is set as the unit length. When considering the Reynolds number effect, the advance coefficient λ remains unchanged by changing the inlet velocity and rotating speed at the same time. If the influence of the advance coefficient is under the consideration, only the rotating speed varies.

As presented in figure 2a, the rectangular computational domain is employed, in which the inlet section extends 4.5R from the rotating centre while the outlet region

is located at X/R=13.5, which is sufficient due to the low inflow turbulence intensity and quick dissipation of the wake flow. The topwall and bottomwall has the same distance of 4.5R based on the centre of the rotating system. The sliding mesh technique by establishing three periodic interfaces, among which two small rotating parts covering two blades are used to accomplish the movement of the airfoils while the large rotating part is adopted to control the motion of the propeller, is completed in commercial code STARCCM +. The hybrid mesh is applied in the computations, involving the prism layer near the airfoil surface and unstructured trimmed mesh in rotating parts and the outer stationary region. To capture the vortical flows, a cone is created to refine the mesh in the wake region. In addition, the meshes in the normal direction to the solid wall and streamwise direction along the airfoil surface are also refined, to resolve the near-wall flow more precisely. The detailed information about the mesh independence can refer to the reference [15]. Finally, 65 layers are placed near the airfoil surface and the total thickness of the prism layer is about 2×10^{-3}m, leading to the distance of the first grid to the wall is about 3.4×10^{-8}m. As a consequence, the non-dimensional y^+ ($y^+=yu_\tau/v$, where y is the distance of the first grid to the wall, u_τ is the friction velocity and v is the kinematic viscosity) on the most part of the airfoil surface does not exceed the value of 0.2.

Table 1 Main geometrical parameters of tested cases

Blade number	2
Blade chord (c/m)	0.0495
Rotor radius (R/m)	0.11
Blade profile	NACA0009, 0012, 0015, 0018, 0022, 2415, 4415, 6415, Inverse NACA2415, 4415, 6415
Pitch-pivot-point (%c)	10, 20, 25, 30, 40, 50, 60
Inlet velocity (U_0/(m/s))	4-10
Rotating speed (n/(r/min))	600-1200
Pitching kinematic ($\theta=\theta_0+\theta_{amp}\sin(\omega t+\pi/2)$)	$\theta_0=5^\circ$, $\theta_{amp}=35^\circ$
Advance coefficient ($\lambda=U_0/(\omega R)$)	0.36-0.72
Reynolds number ($Re=\sqrt{{U_0}^2+(\omega R)^2}c/\nu$)	2.85×10^4-7.11×10^4
Vertical force coefficient C_{VF}	$C_{VF}=F_{VF}/(0.5*\rho*U_0^2*c)$
Propulsive force coefficient C_{PF}	$C_{PF}=F_{PF}/(0.5*\rho*U_0^2*c)$
Power coefficient C_{power}	$C_{power}=P/(0.5*\rho*U_0^3*D*H)$
Efficiency (η/%)	$\eta= F_{PF}*U_0/P$

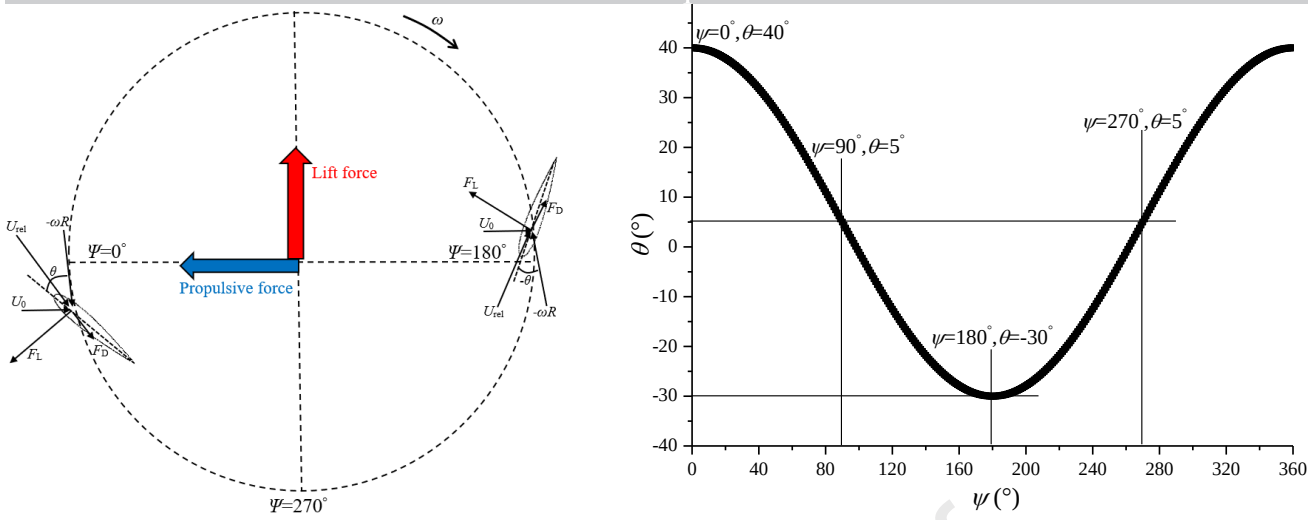

(a) (b)

Figure.1 Motion of the cycloidal rotor and variation of the pitch angle in a revolution. (a) Rotating trajectory of two blades; (b) Change of pitch angle in a rotating cycle.

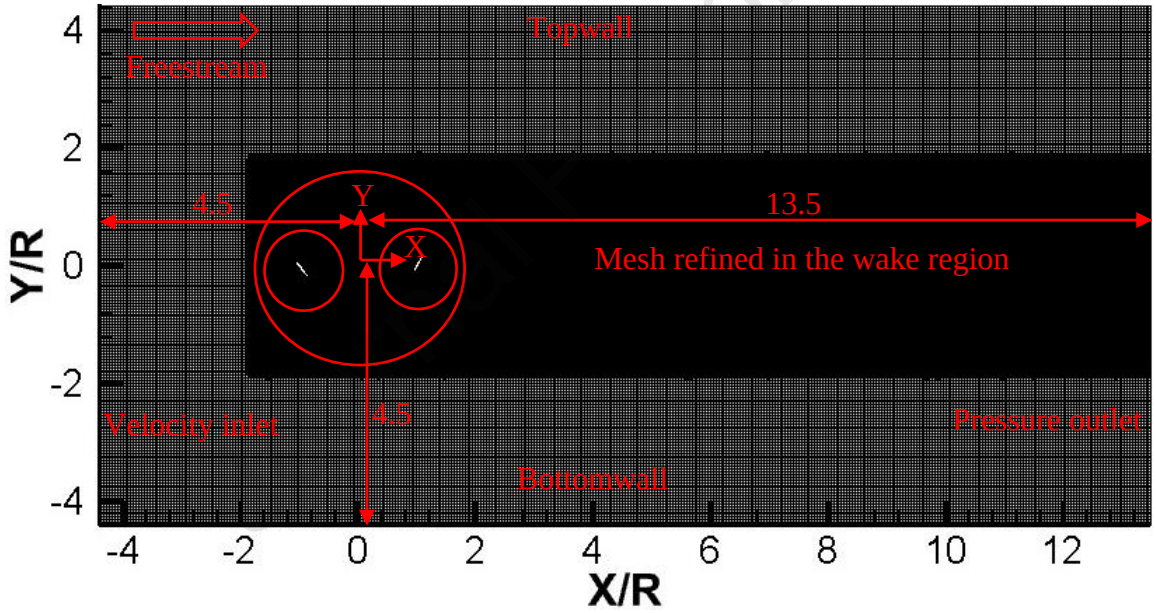

(a)

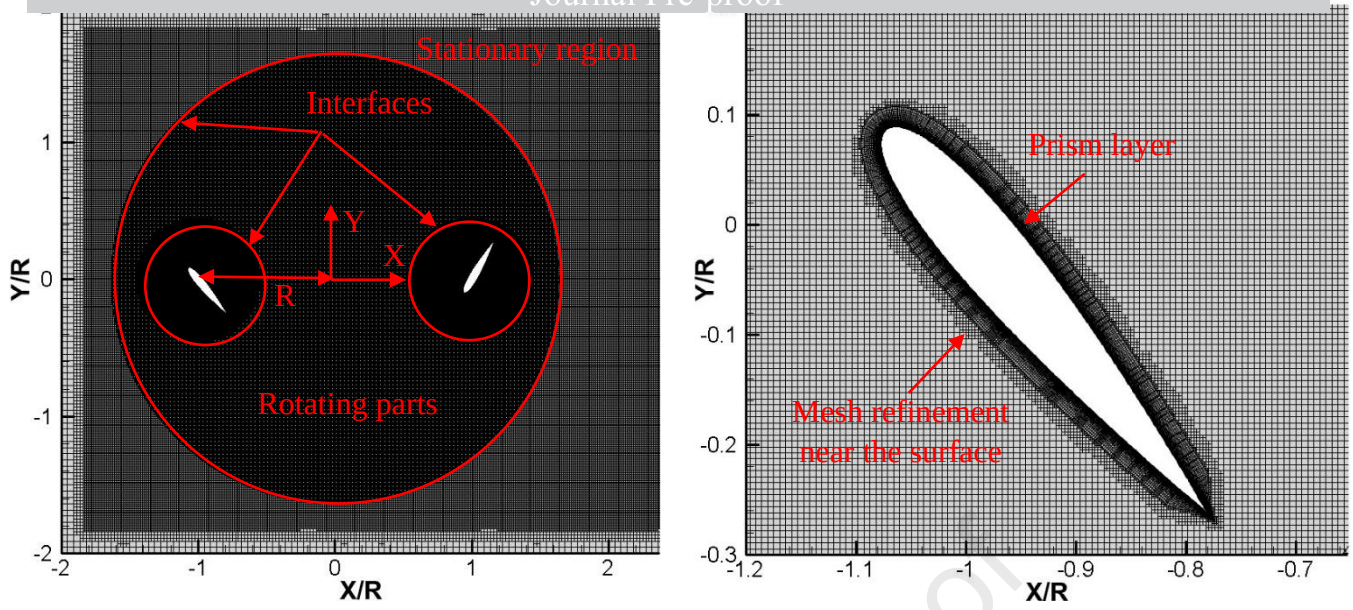

(b) (c)

Figure.2 Computational configuration and mesh generation. (a) Mesh in the whole computational domain; (b) Mesh in the rotating parts; (c) Mesh near the airfoil surface.

2.2 Boundary conditions and numerical setup

The two-dimensional incompressible unsteady flow is solved by the commercial code STARCCM +. The second-order upwind scheme is applied to the convection term while the second-order backward Euler method is employed to the temporal discretization. The turbulence model is SST $\gamma - \overline{Re}_{\theta t}$ transition model to consider the transition effect at low Reynolds number condition. Rezaeiha et al. [16] tested a series of RANS-based turbulence models with application to the vertical-axis wind turbine, and concludes that only the SST model variants can get the good results compared with the experiments. Simultaneously, the transitional SST versions are recommended in the transitional regime. In our previous work [15], the results show that the SST $\gamma - \overline{Re}_{\theta t}$ transition model is indeed superiority to predicting the global performance of the cycloidal rotor. The boundary condition, including the inlet velocity and pressure outlet, is employed. The turbulence intensity is 0.25% corresponds to the experimental measurement [17] and the eddy viscosity ratio is 0.001 due to the low Reynolds number. The wall y^+ wall treatment is selected because it is appropriate for a variety of mesh densities. To get the converged results, 15 rotations are necessary and the flow structure in the last one is analyzed. The influence of the mesh, turbulence model, inlet flow condition, wall function, timestep, inner iteration loops and number of the rotation are investigated in the related work [15].

3. Validation of the numerical results

The numerical results in the present work are compared with the work obtained by Spalart-Allmaras $\gamma - \overline{Re}_{\theta t}$ transition model (SA TM) in reference [17]. According to the performance curves of the single blade in figure 3, it seems that the vertical force coefficient in advancing side at ψ=240˚-360˚ has large difference compared with the available computations, but the distributions of propulsive force and power coefficients are quite similar. It is interesting that at nearly ψ=320˚-360˚ and 0˚-90˚, the propulsion system achieves the negative power coefficient, which means that it can extract the energy from the working fluid. However, the location where the power coefficient has the negative value remains unchanged with the increase of the advance coefficient. In addition, the variation of the performance becomes small at high advance coefficient. In conclusion, it seems that our numerical results can predict the performance well, and some discrepancy can be ascribed to the choice of the turbulence model and mesh arrangement in previous computations.

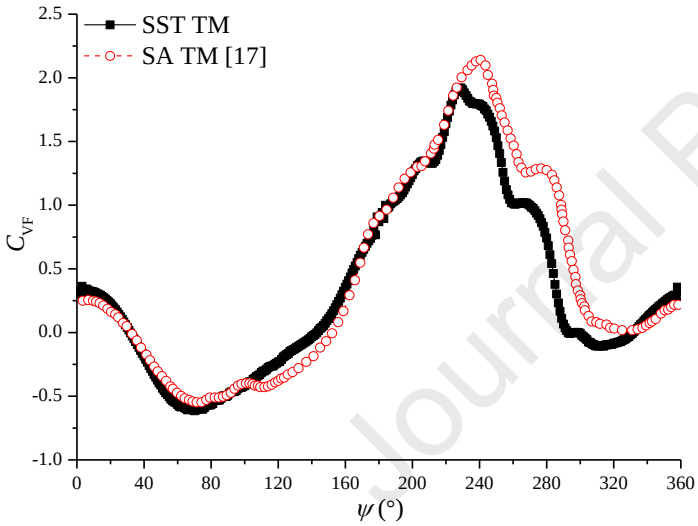

(a)

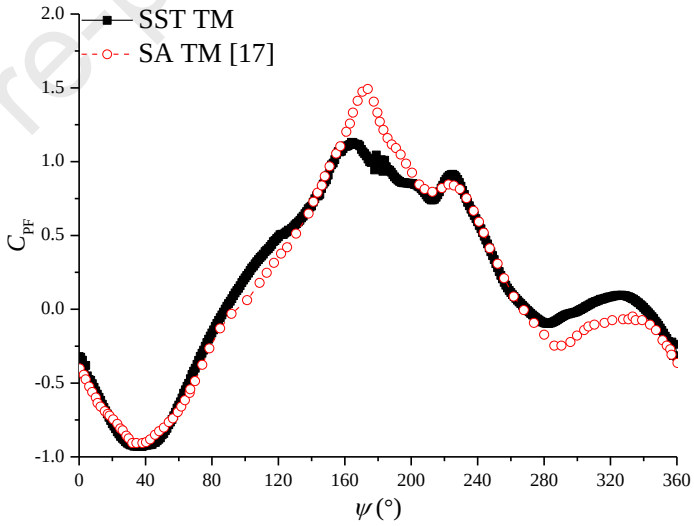

(b)

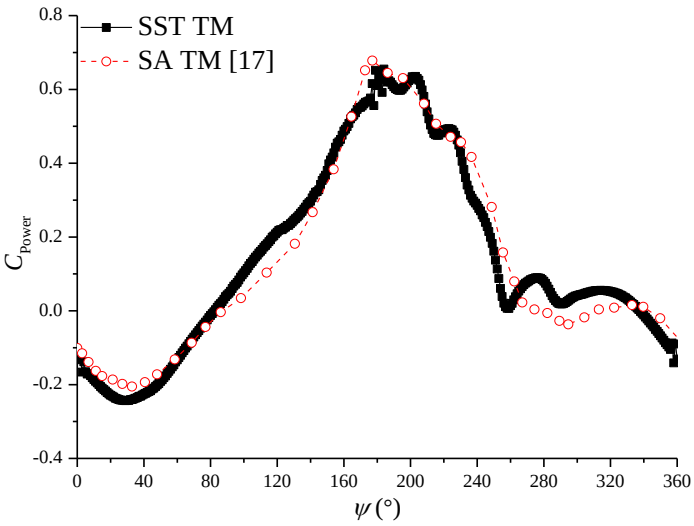

(c)

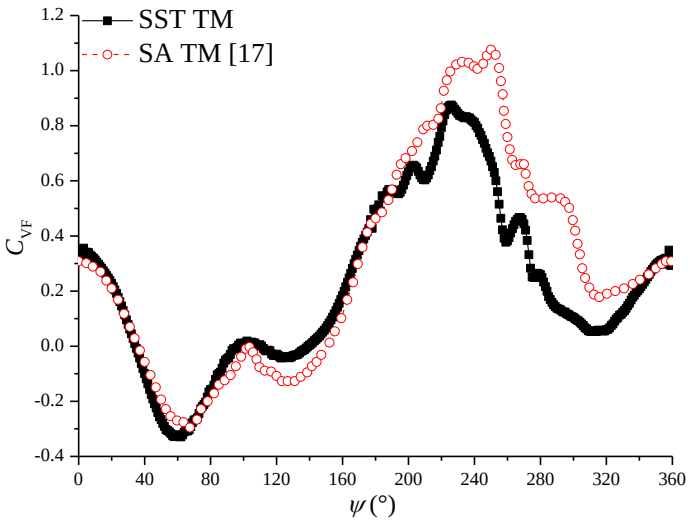

(d)

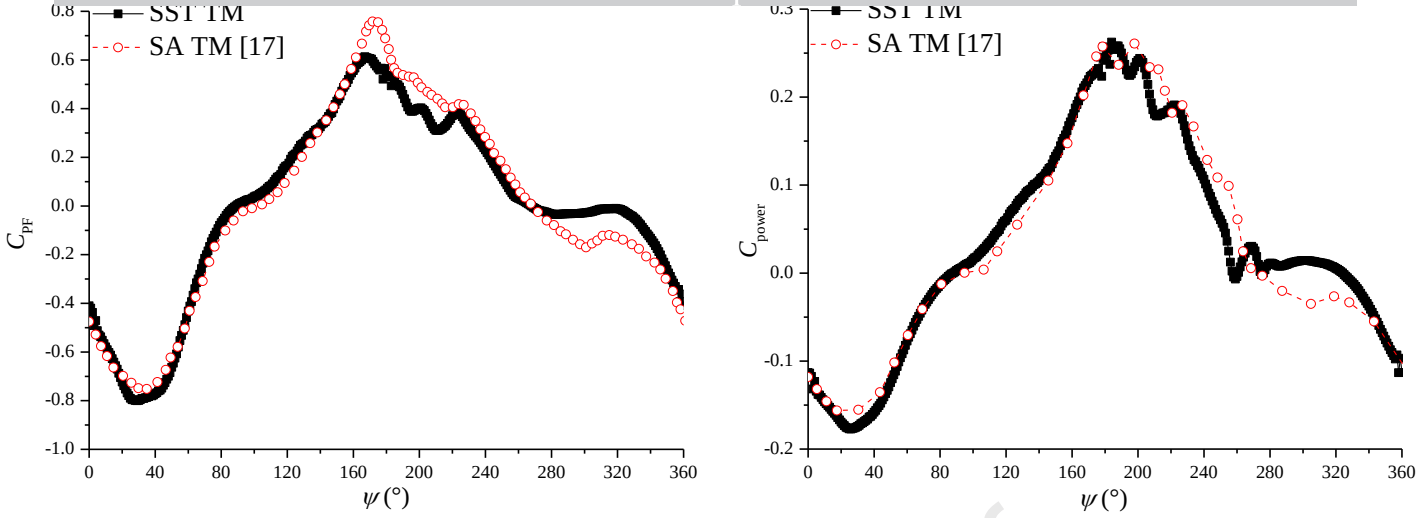

(e) (f)

Figure.3 Performance curves. (a), (b) and (c) Vertical force, propulsive force and power coefficients at λ=0.52; (d), (e) and (f) Vertical force, propulsive force and power coefficients at λ=0.73.

The internal flow structures are also used to compare with the particle image velocimetry (PIV) measurements at different azimuthal angles under two advance coefficient conditions. The experimental work was performed in a closed-section wind tunnel in University of Maryland [17]. The flow structure is captured by tracing the vaporized mineral oil seeded at the inlet section and the velocity filed measurements are located at the mid-span of the cycloidal rotor, which can eliminate the three-dimensional effect. The non-dimensional spanwise vorticity contours ($\omega_z c/U_0$) at λ=0.52 are displayed in figure 4 to analyze the gross feature of the unsteady vortical flow inside the 2-bladed cycloidal rotor. At ψ=0°, there is a strong interaction between the wake B and blade B near the leading edge. Then, when the azimuthal angle increases to 30°, the main flow structures are wake B-wake B and wake A-blade B interactions. Afterwards, except for the obvious wake B-wake B interaction, it also has the wake A-wake B interaction near the trailing edge of blade B. Although the general flow field is obtained by the present work, there still has some difference between the experiments and computations. For an instance, in figure 4d, wake A has evident interaction with the leading edge of blade B, but this does not occur in figure 4c, which means that the trajectory of the wake has relatively large discrepancy.

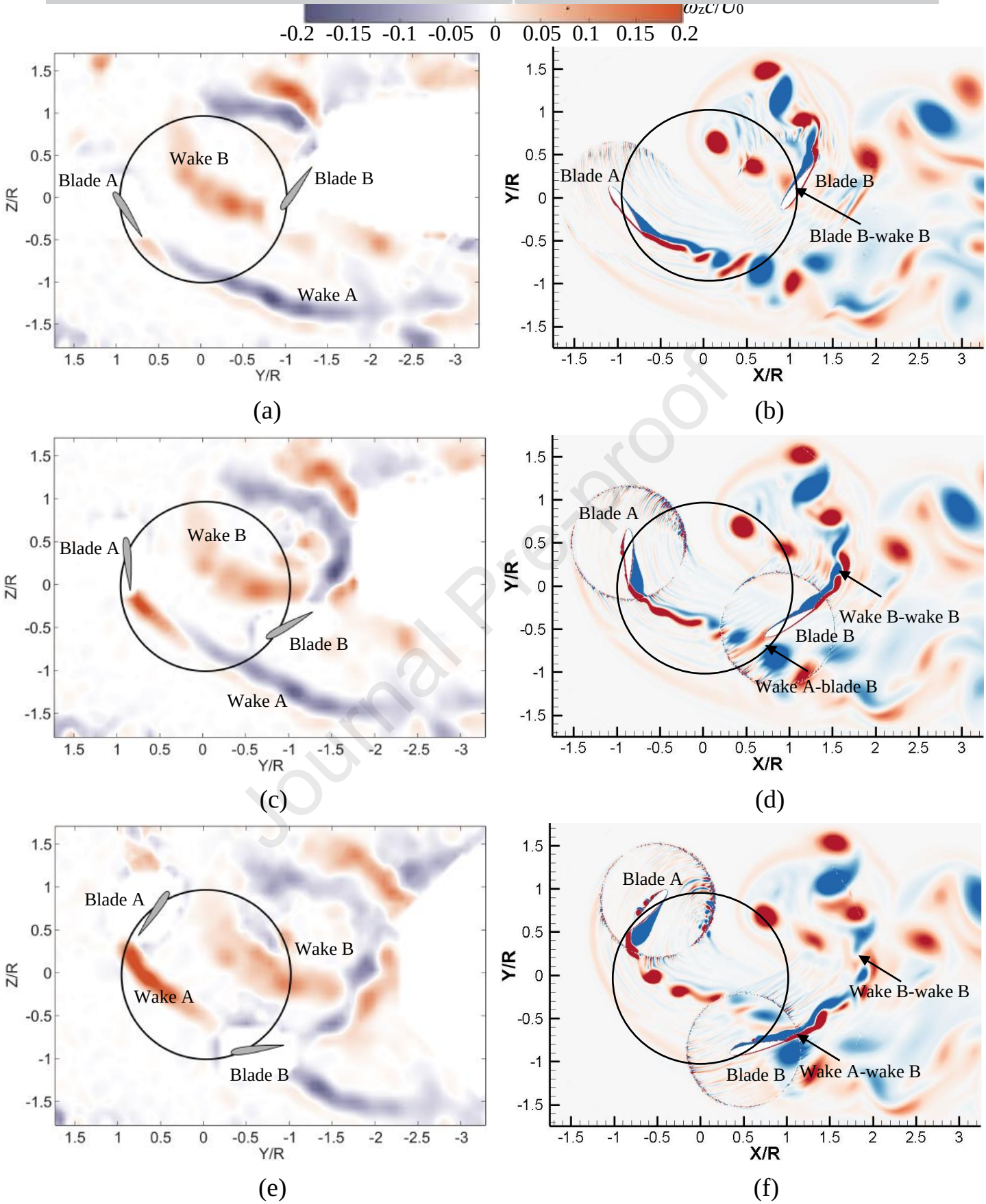

Figure.4 Flow structures at λ=0.52. (a) and (b) ψ=0˚; (c) and (d) ψ=30˚; (e) and (f) ψ=60˚.

4. Results and discussion

4.1 Effect of the pitch-pivot-point

In this section, the influence of the pitch-pivot-point on the performance and flow structures are investigated systematically. Seven pitching locations from x/c=0.1 to 0.6, are employed in the present work. Figure 5 shows the overall performance of the rotating system at different Reynolds number, by changing the inlet velocity and rotating speed simultaneously to remain the advanced coefficient unchanged. It should be noted that the lift coefficient of the cycloidal rotor is in Y direction, and is defined as $C_L=F_L/(0.5*\rho*U_0^2*c)$ (where F_L is the sum of the vertical forces provided by each blade). It seems that increasing the Reynolds number increases the lift coefficient, but decreases the propulsive force and power coefficients. At a constant Reynolds number, the lift coefficient increases as the pitch-pivot-point moves towards the leading edge, but it shows the opposite trend for the propulsive force and power coefficients. It is observed that the system produces the largest propulsive force when the pitch-pivot-point is located at x/c=0.5, but the efficiency is relatively low due to the large power consumed. According to the distribution of efficiency, it seems that the highest performance appears when the pitch-pivot-point ranges from 0.25 to 0.3 under various Reynolds number conditions. Simultaneously, as the pitching point is close to the middle chord, the performance becomes worse, because of the high consumption of the power.

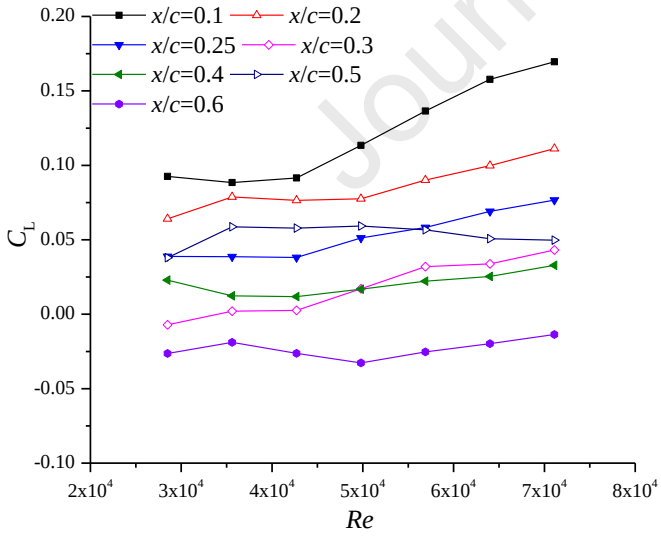

(a)

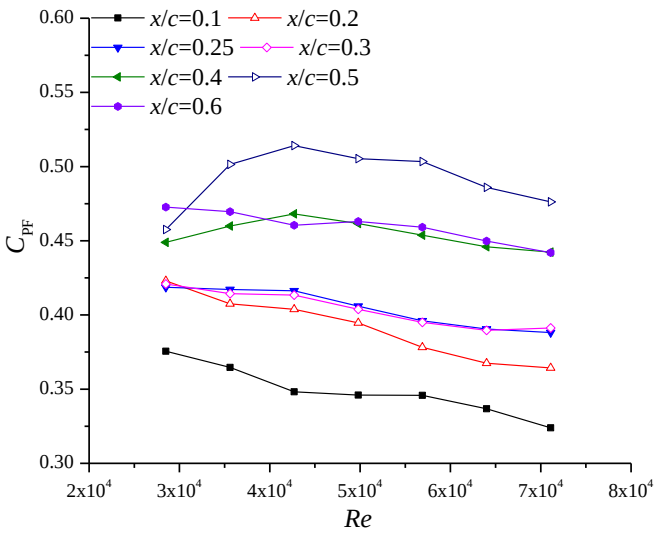

(b)

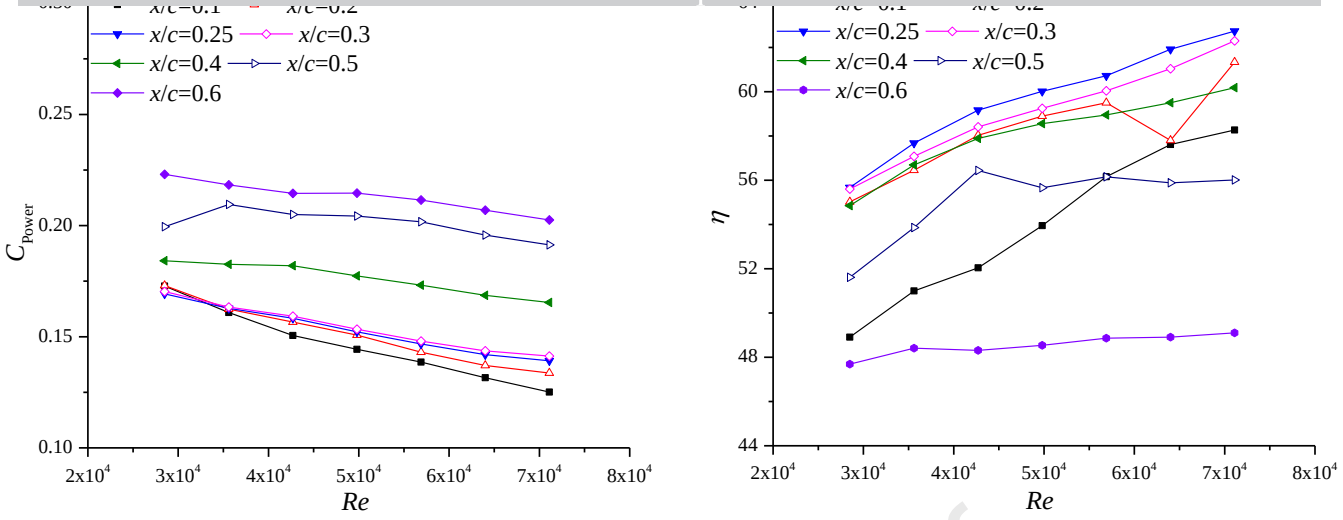

(c) (d)

Fig.5 Time-averaged performance of the cycloidal rotor with different pitch-pivot-point. (a) Lift coefficient; (b) Propulsive force coefficient; (c) Power coefficient; (d) Efficiency.

The spanwise vorticity contours of cases with various pitching points are displayed in figure 6 to show the general flow field at ψ=0°. At this position, blade B has the high risk in interacting with wake B, especially when the pitching point approaches to the middle chord. Moreover, the vortical flows become more complicated for cases with x/c=0.4, 0.5 and 0.6, which makes the contribution to the large power in figure 5c. Besides, it is observed that the massive flow separation on the left side of blade A and right side of blade B appear violently, leading to the more disordered wakes. Consequently, it concludes that the general flow field becomes more chaotic as the pitching point moves to the blade trailing edge, shown by the substantial flow separation on one side of two blades and more unsteady wakes. Indeed, moving the pitch-pivot-point can be regarded as adding a plunging motion to the original pitching motion, which changes the resultant wake flows, as was reported by Tian et al. [2]. In addition, Li et al. [18] observed that the LEV occurs earlier and the lift coefficient becomes larger, when the pitching point reaches to the leading edge of a pitching airfoil during the upstroke process, which is consistent with the current study. However, in the cycloidal rotor, the investigations associated with the pitch-pivot-point effect are extremely rare.

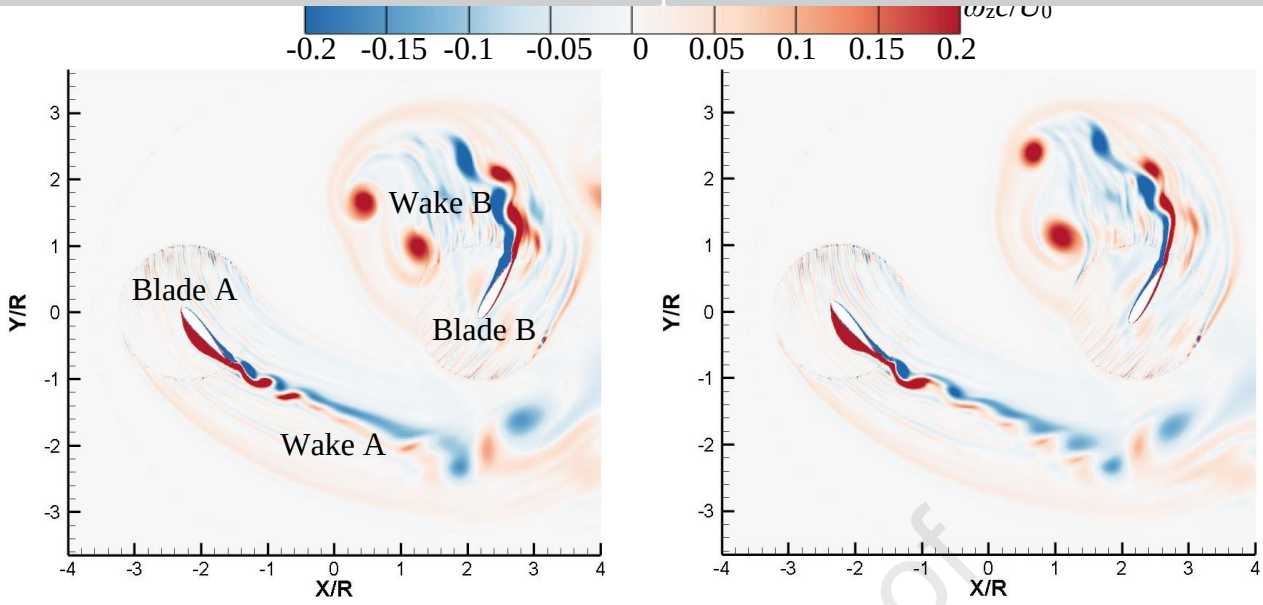

(a)

(b)

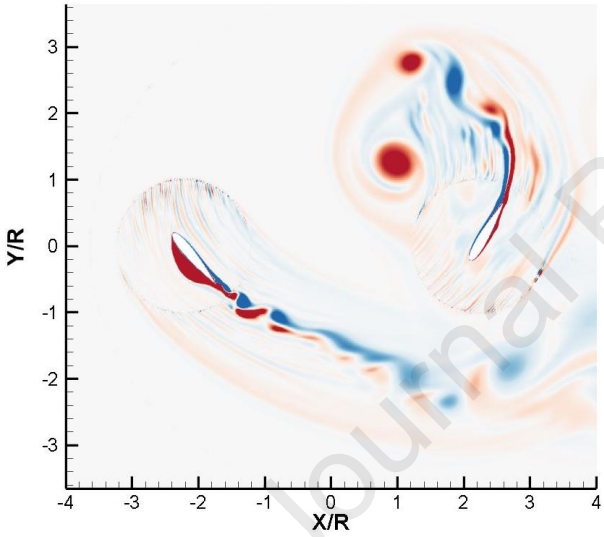

(c)

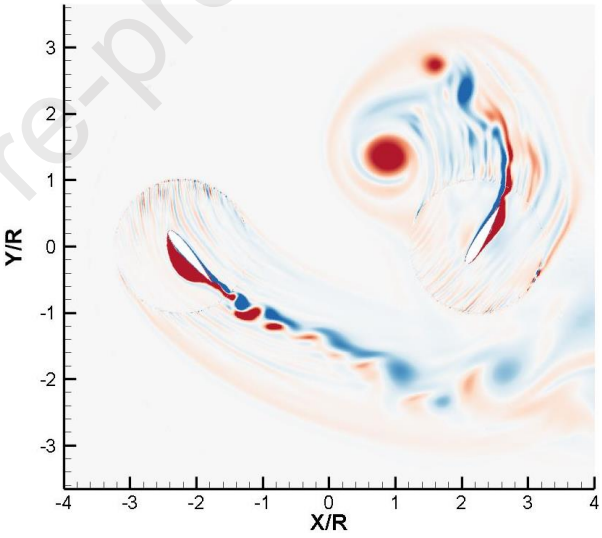

(d)

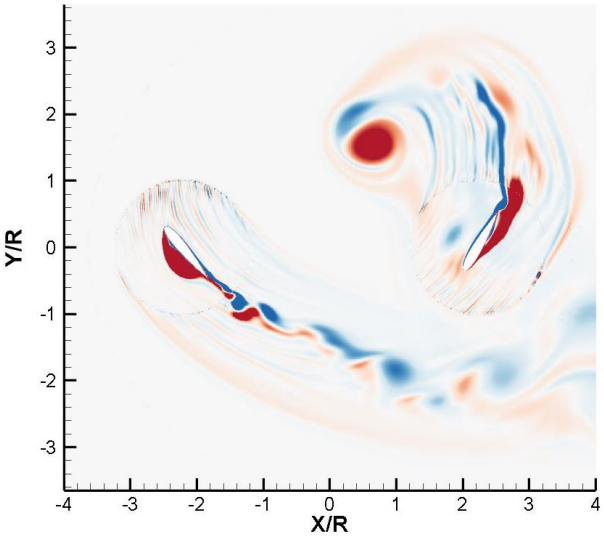

(e)

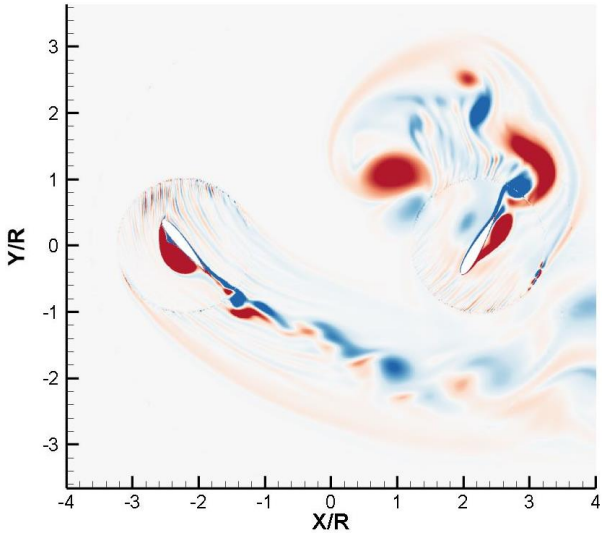

(f)

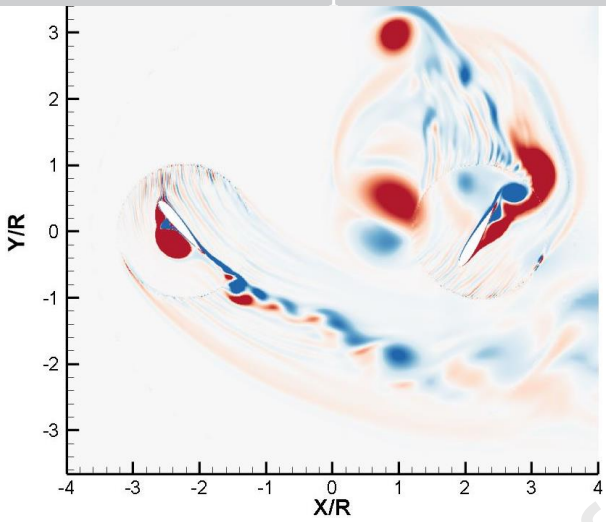

(g)

Fig.6 Flow structures of cases with different pitch-pivot-points. (a) x/c=0.1; (b) x/c=0.2; (c) x/c=0.25; (d) x/c=0.3; (e) x/c=0.4; (f) x/c=0.5; (g) x/c=0.6.

At λ=0.52 and Re=4.98×10^4, three locations of x/c=0.25, 0.5 and 0.6, are adopted to study the effect of the pitch-pivot-point on the performance of the rotating system and single blade, as well as the internal flow structures. Figure 7 plots the performance curves of different cases. When the pitching point is located at x/c=0.6, the time-averaged lift coefficient of the cycloidal rotor is negative because of the large magnitude from ψ=120° to 180°. Besides, in figure 7b, the distribution of the propulsive force coefficient is extremely different, especially for the case with x/c=0.25. According to the performance of the single blade in a revolution, it is found that the performance variation of the case with x/c=0.25 is relatively large compared with that of other two cases. As a consequence, the azimuthal angle ψ=170° is selected to clarify the difference of the lift and propulsive force coefficients for three cases.

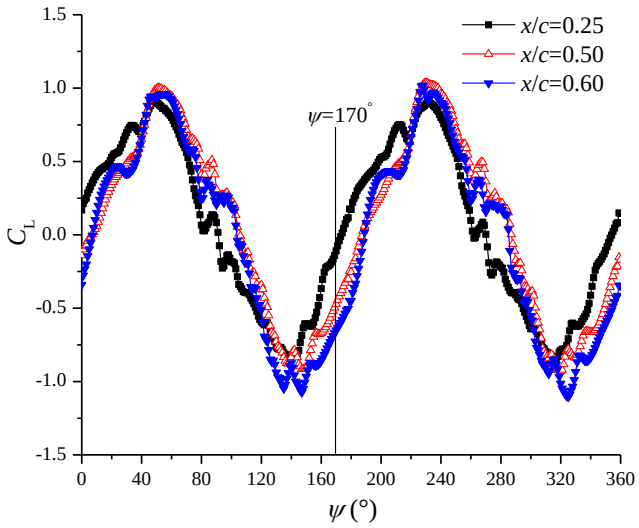

(a)

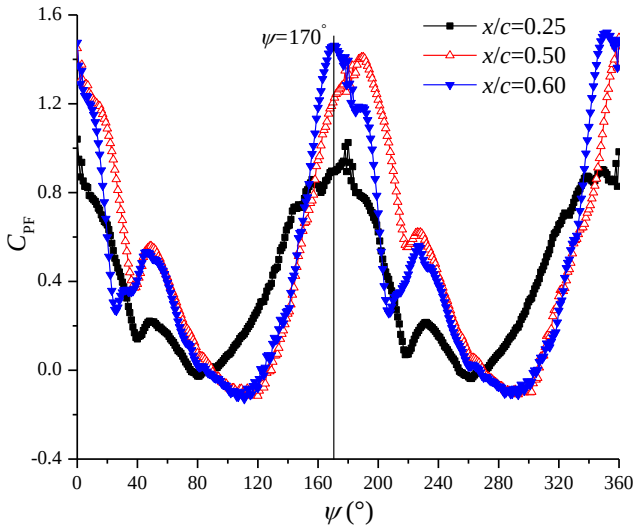

(b)

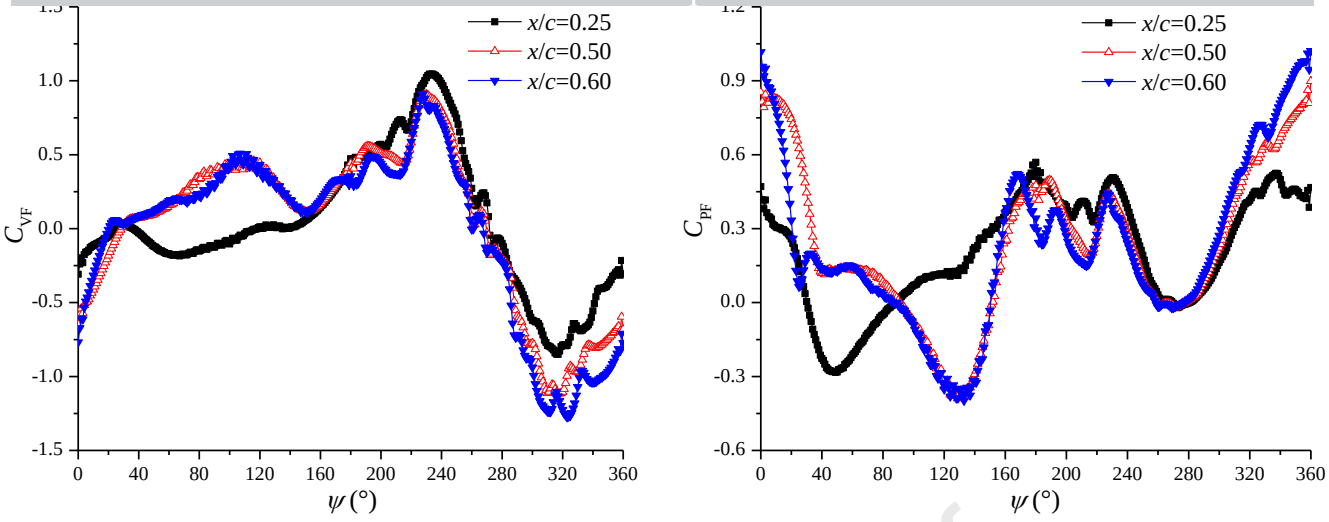

(c) (d)

Fig.7 Performance of the cycloidal rotor and single blade. (a) Lift coefficient of the rotating system; (b) Propulsive force coefficient of the rotating system; (c) Vertical force coefficient of the single blade; (d) Propulsive force coefficient of the single blade.

Both the time-averaged lift and propulsive force coefficients of the cycloidal rotor have much difference at ψ=170° for cases with various pitching points. In figure 8a, 8b and 8c, the general flow field shows that there is a strong blade A-wake A interaction as the pitch-pivot-point moves towards the middle chord. In addition, the massive flow separation is more obvious on the left side of blade B and right side of blade A, for cases with x/c=0.5 and 0.6. When considering the distributions of C_p ($C_p=p/(0.5*\rho*U_0^2)$, where p is the local pressure) on two blades, it seems that the main difference is the pressure on the left side of blade A due to the stagnation point location, and the pressure on the right side induced by an attached vortex, presented by the non-dimensional velocity contours (U/U_0) in figure 8f, 8g and 8h. Evidently, with the pitch-pivot-point moving to the middle chord, the size of this vortex becomes larger. Although the pressure distributions and flow structures over the surface of blade A are different for three cases, the resultant vertical force in figure 7c is quite similar because of the relatively small blade loading. For blade B, the pressure difference is much larger than blade A, as shown in figure 8e. The flow structure shows that a large-scale LEV attaches on the suction side, which has great impact on the pressure there. The LEV has larger size as the pitching point moves towards the middle chord, bringing about the large magnitude of negative vertical force in figure 7c. Thus, the mean lift coefficient difference of three cases is mainly caused by blade B, resulting from the attached large-scale LEV.

According to the variation of the propulsive force coefficients of the rotating system and single blade, it can be seen that the contribution of blade A can be neglected because of the relatively small blade loading in figure 8d, although it can produce the positive propulsive force as a result of the upward lift. As a main

contributor, blade B produces the large positive propulsive force induced by the downward lift, because of the large pressure difference in figure 8e. A sketch of the forces acting on two blades and the rotating system is shown in figure 8j, to help understand how the single blade makes the contribution to the force generation of the cycloidal rotor. Therefore, the main conclusion is that blade B is responsible for the difference of both mean lift and propulsive force coefficients of the rotating system for three cases with various pitch-pivot-point.

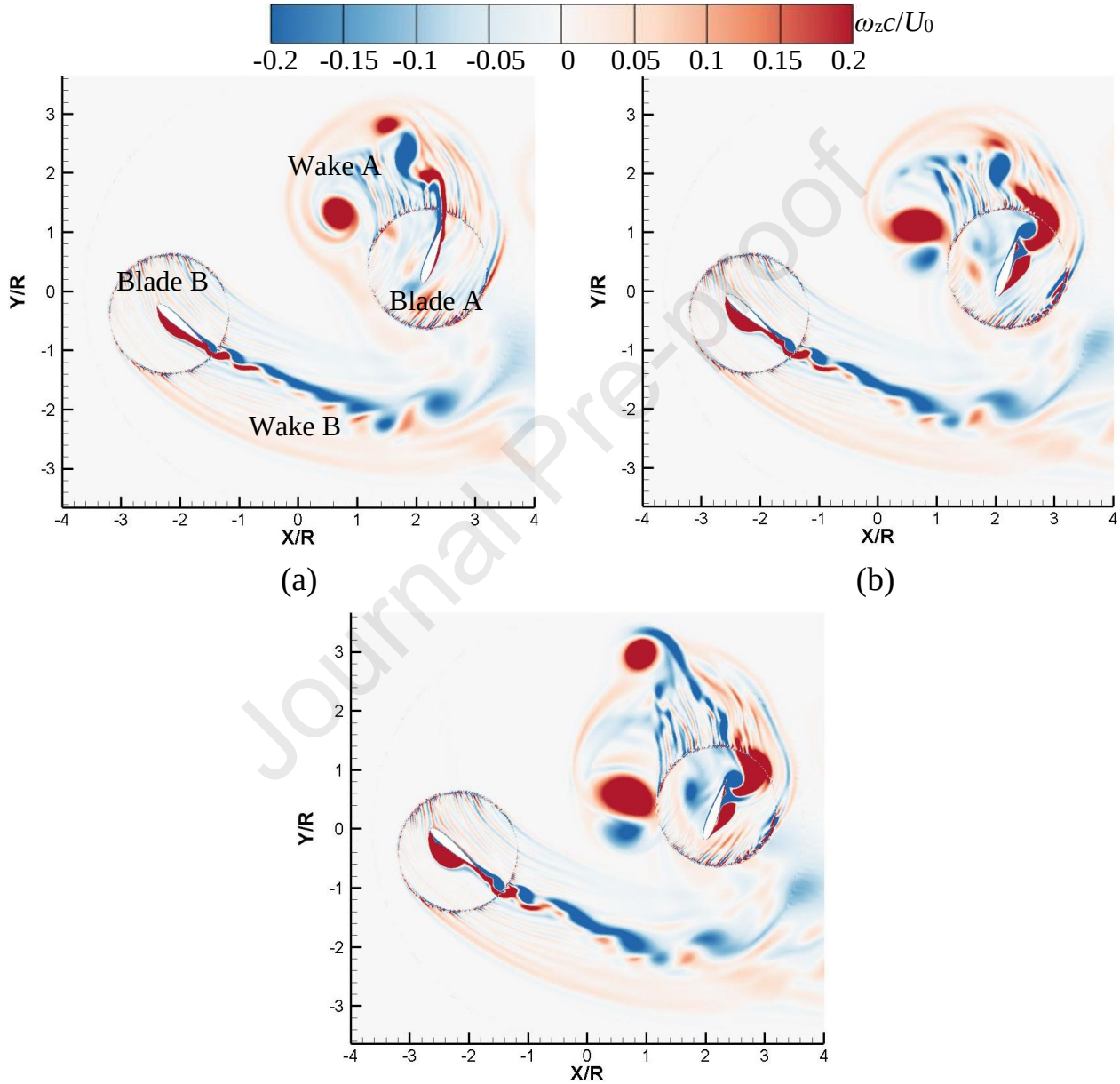

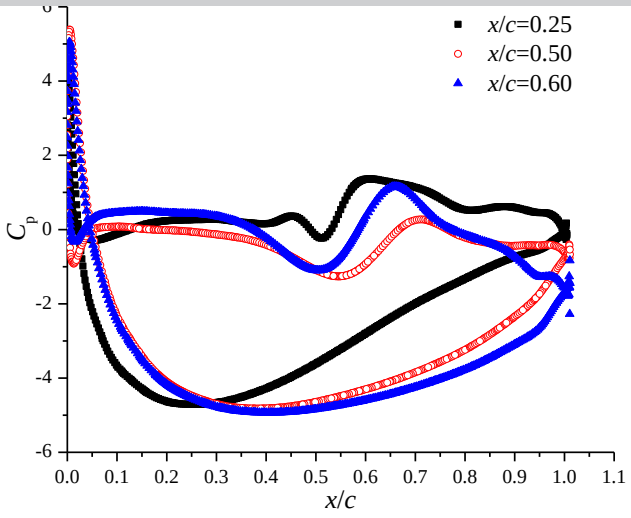

(d)

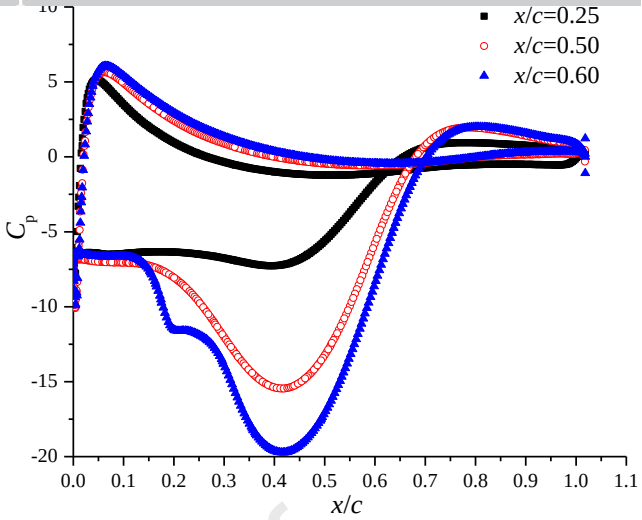

(e)

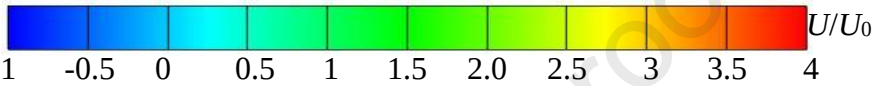

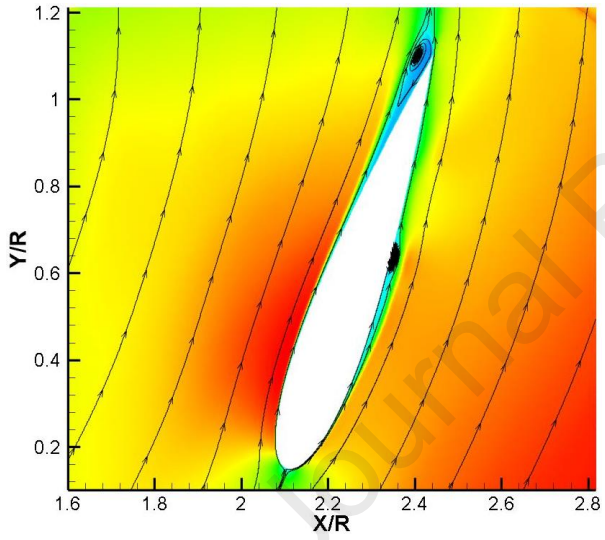

(f)

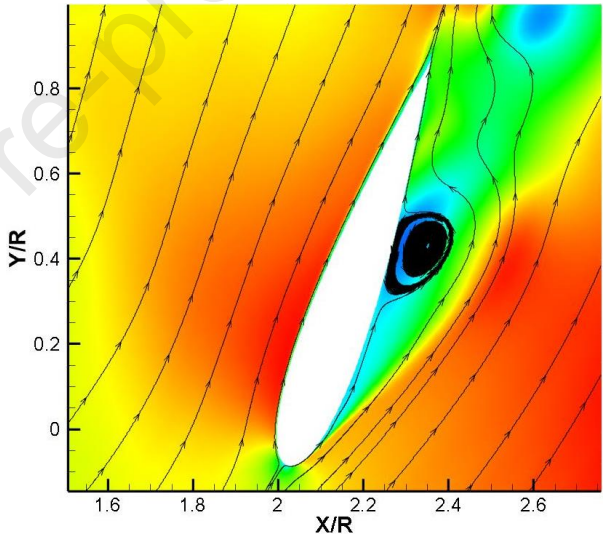

(g)

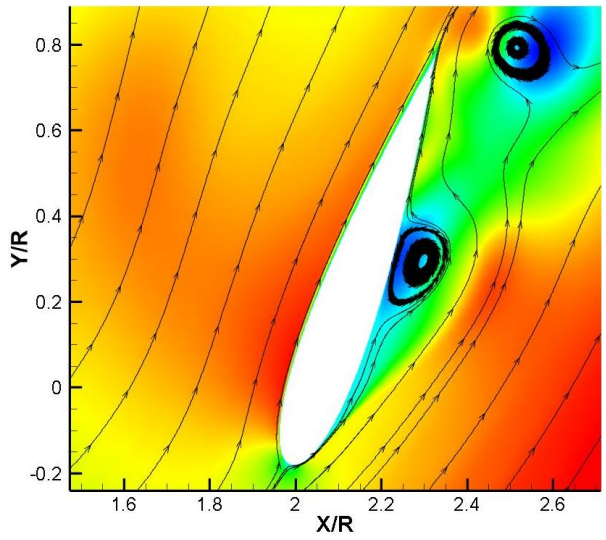

(h)

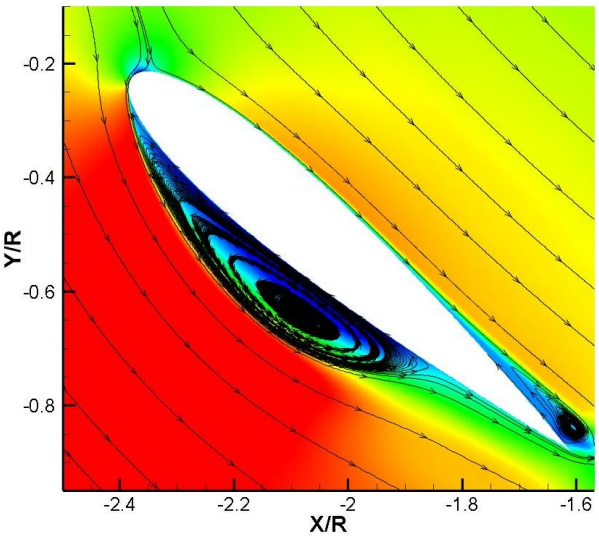

(i)

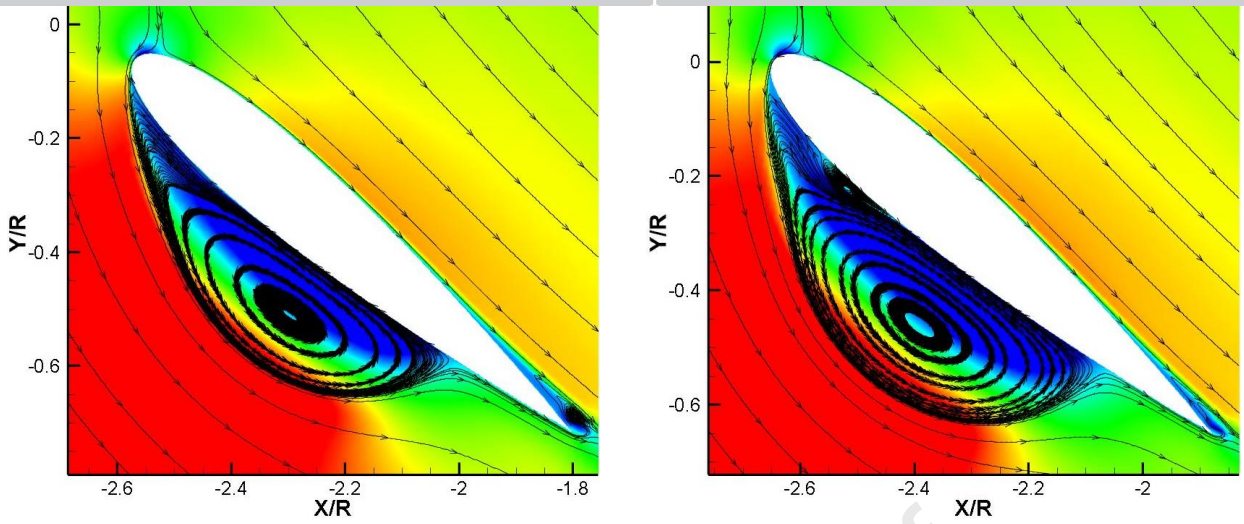

(j)

(k)

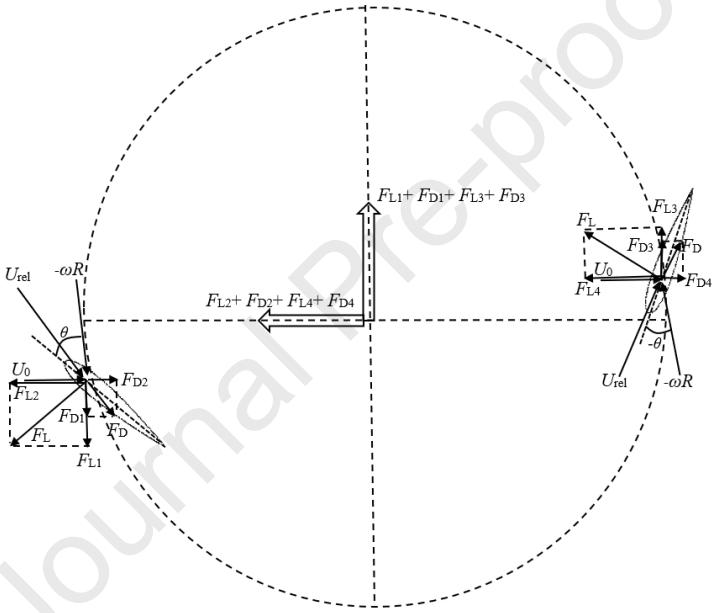

(l)

Fig.8 Flow structures and blade loadings of two blades at ψ=170°. (a) Global flow structure of the case with x/c=0.25; (b) Global flow structure of the case with x/c=0.5; (c) Global flow structure of the case with x/c=0.6; (d) Pressure distribution of blade A; (e) Pressure distribution of blade B; (f) and (i) x/c=0.25; (g) and (j) x/c=0.5; (h) and (k) x/c=0.6; (l) Sketch of the forces on two blades and the rotating system.

4.2 Effect of the blade profile

In this section, the influence of the blade profile on the performance of the cycloidal rotor is discussed thoroughly. Eight blade profiles, involving NACA0009, 0012, 0015, 0018, 0022, 2415, 4415 and 6415, are adopted in this work. The first five have the symmetrical geometry while NACA2415, 4415 and 6415 are asymmetrical profiles modified based on NACA0015. In addition, the influence of the inverse NACA2415, 4415 and 6415 profiles are also studied by changing the

geometry placement. The time-averaged overall performance of the cycloidal rotor with various blade profiles under different Reynolds number conditions are plotted in figure 9. It is observed that the asymmetrical profile can produce the higher lift coefficient with the increase of *Re*. For the symmetrical profile, such as NACA0009, 0012 and 0015, the obtained lift coefficient remains nearly unchanged with *Re*. However, the lift coefficients obtained by NACA0018 and 0022 have a significant increase as *Re* increases, which is more obvious for NACA0022. When it comes to the inverse asymmetrical profile, it can be seen that the lift coefficient of inverse NACA6415 decreases remarkably with *Re*. The distribution of the propulsive force coefficient shows a similar trend for various profiles, except for inverse NACA4415 and 6415. At a fixed *Re*, NACA6415 gets a highest propulsive force coefficient, followed by the other two asymmetrical and four symmetrical profiles. Although the asymmetrical profiles obtain the higher propulsive force coefficient, the power coefficient of the rotating system is also higher, which directly leads to the low efficiency, as shown in figure 9d. Additionally, the propulsive force efficiency achieved by symmetrical profiles is much higher, because of the relatively high propulsive force and low power. A very interesting phenomenon is that the inverse NACA2415 has the highest efficiency under high Reynolds number condition, due to the significant decrease of the power coefficient.

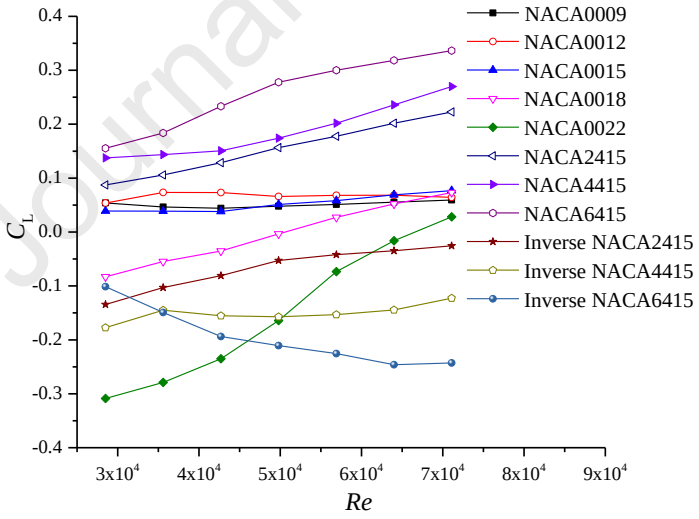

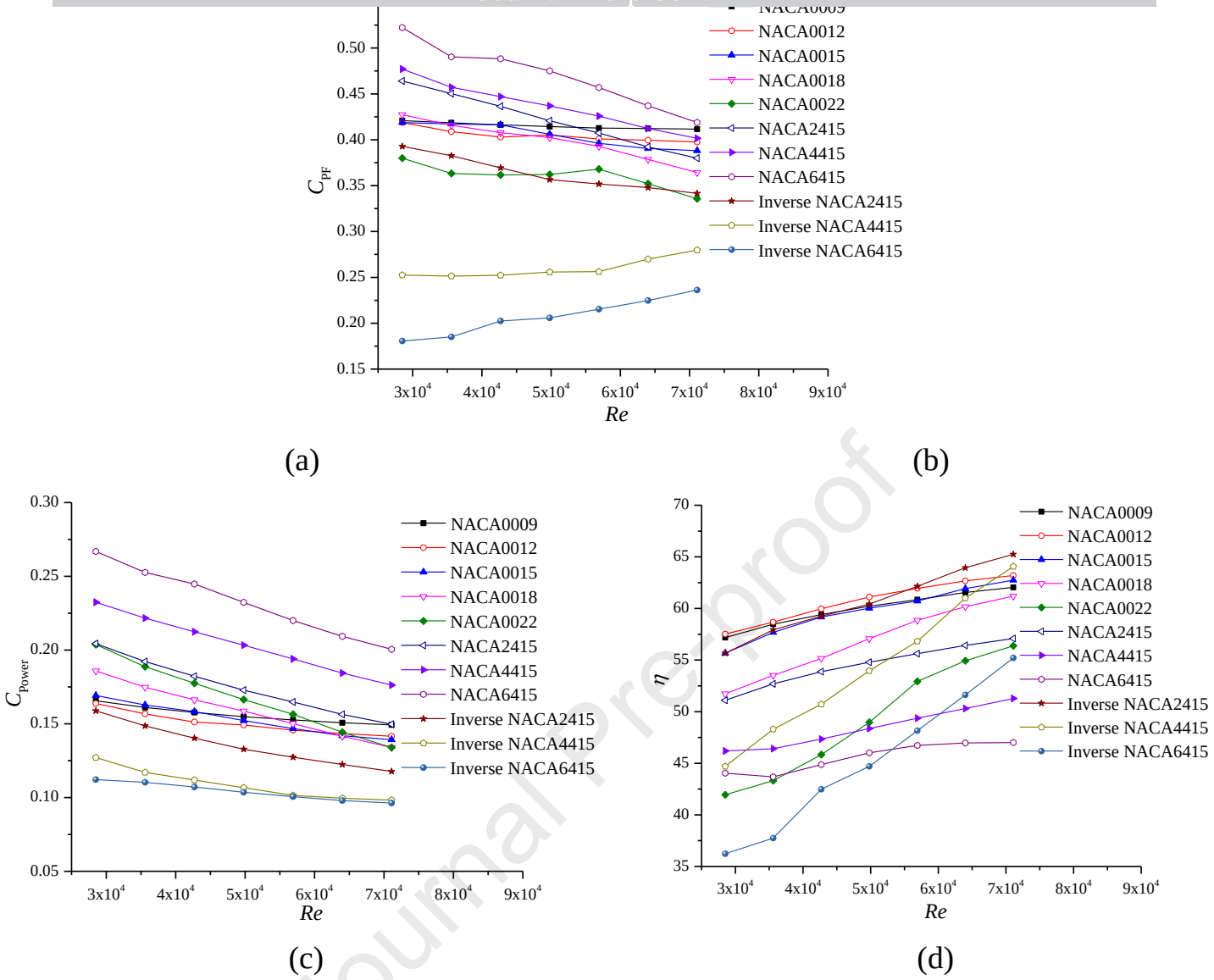

Fig.9 Time-averaged performance of the cycloidal rotor with different blade profiles. (a) Lift coefficient; (b) Propulsive force coefficient; (c) Power coefficient; (d) Efficiency.

Then, the flow structures of the two-bladed cycloidal rotor with different blade profiles, involving the symmetrical and asymmetrical ones, are displayed in figure 10 at ψ=0°. As the thickness of the symmetrical profile increases, the vortical flows have different patterns. There is almost no much difference in flow filed for NACA0009, 0012 and 0015. However, for NACA0018 and 0022, the wakes are more unsteady and the flow separation is more obvious on the left side of blade A. Obviously, the wake B is closer to blade B for NACA0022, which indicates that flow separation occurs earlier. Moreover, the wakes shedding from the asymmetrical profile is more disordered and there exists the massive flow separation on the left side of blade A and right side of blade B, especially for NACA6415, which should be responsible for the high consumption of the power in figure 9c. When the asymmetrical profile is in inverse mode, it seems that the vortical flows are suppressed and the consumed power in figure 9c is evidently decreased. Though the

flow separation on the left side of blade A is still visible, it almost disappears on blade B, as well as the wake B for inverse NACA6415.

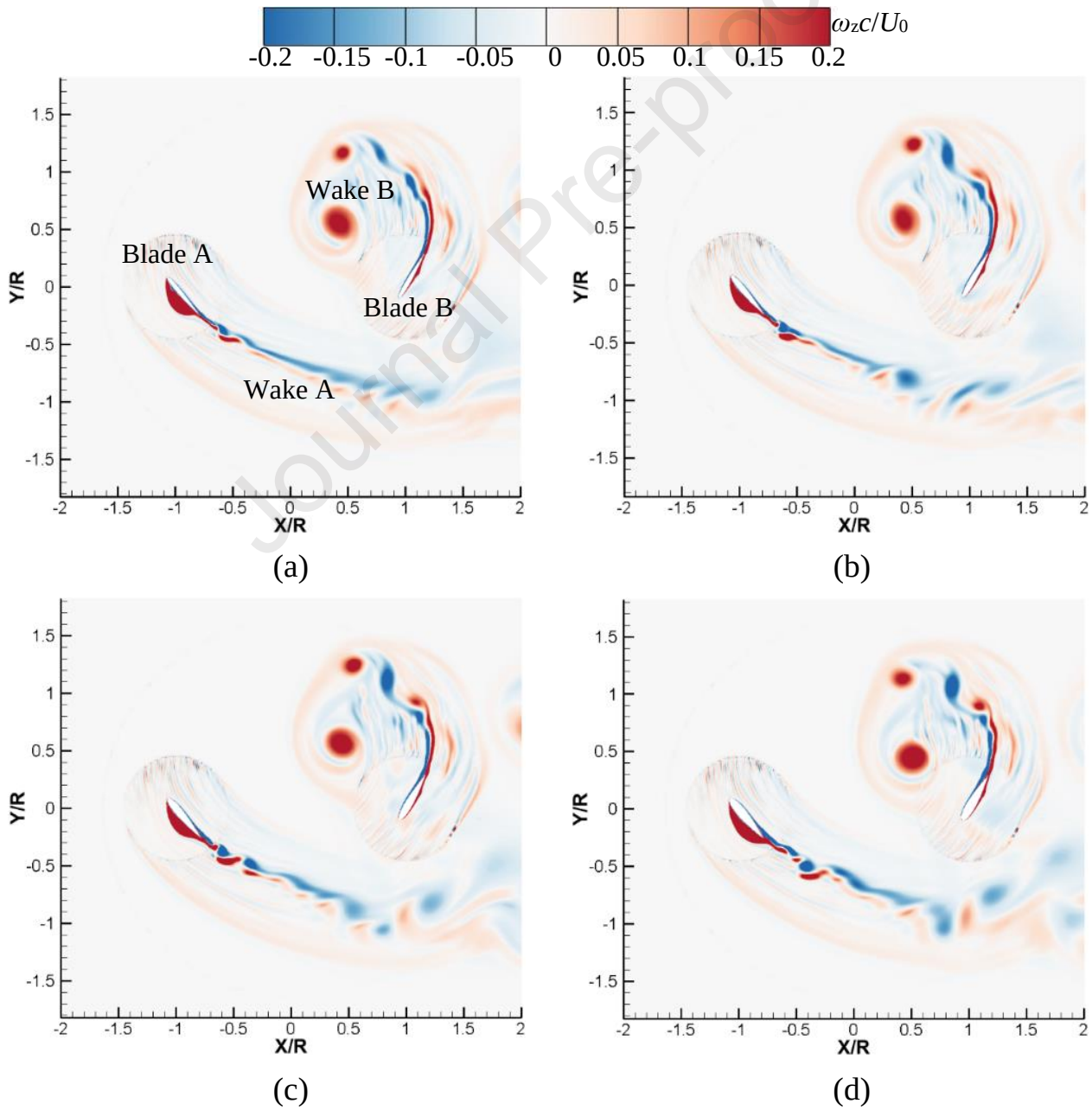

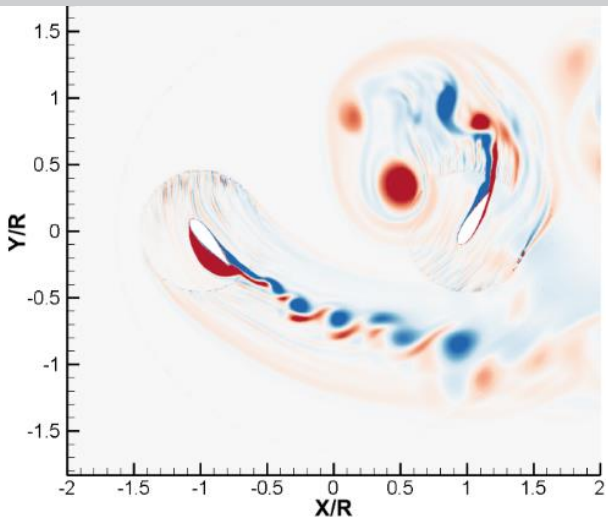

(e)

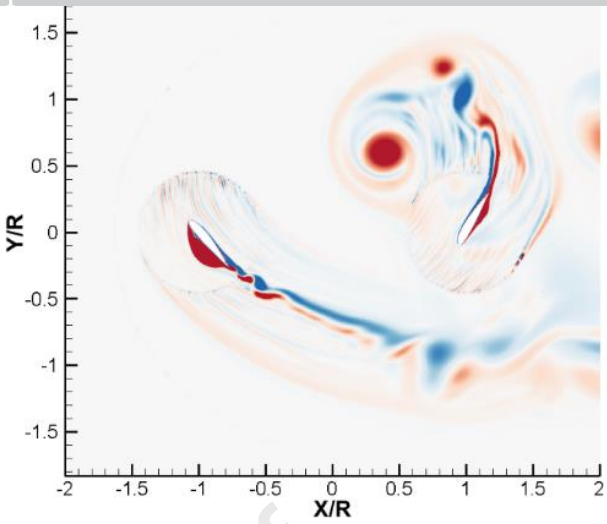

(f)

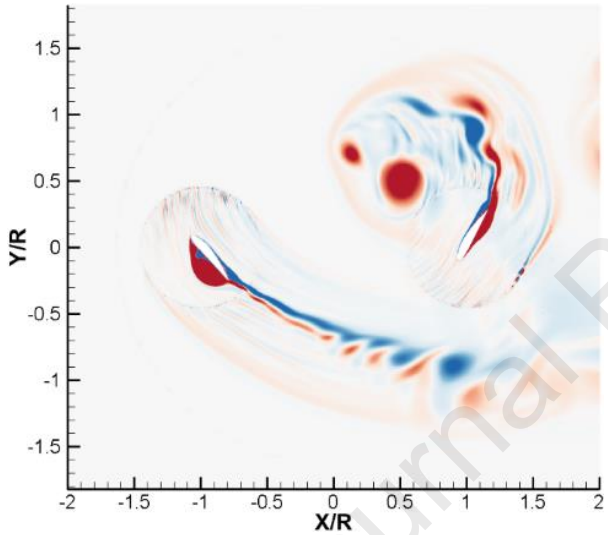

(g)

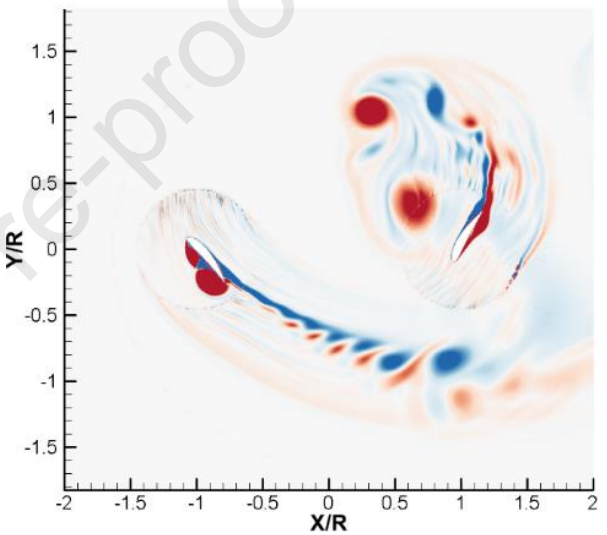

(h)

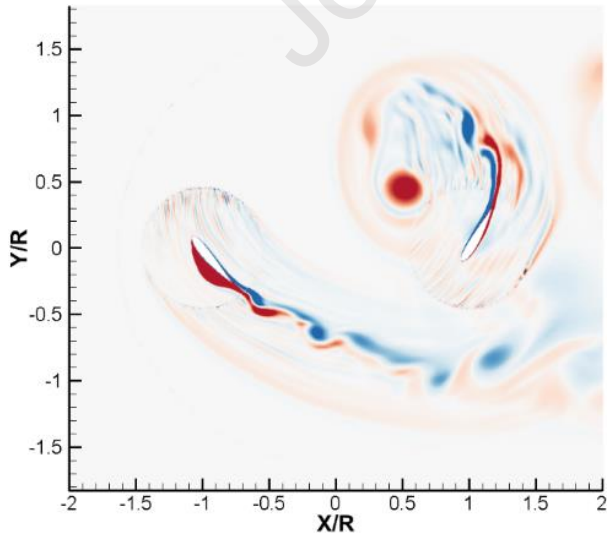

(i)

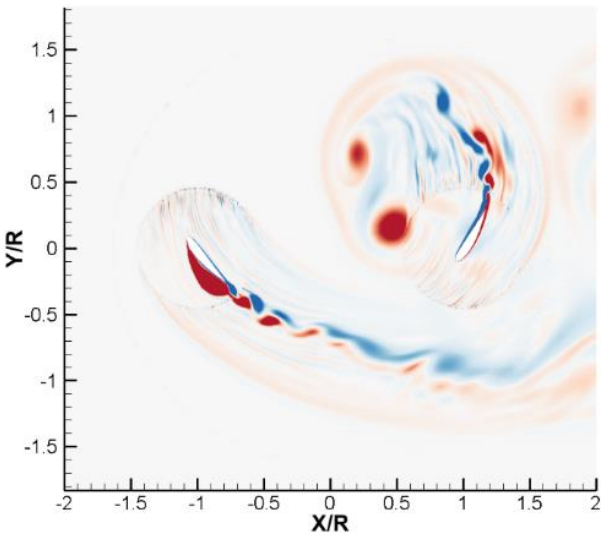

(j)

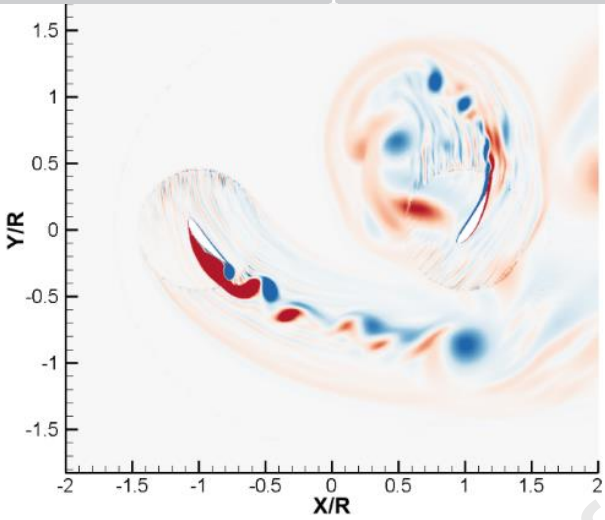

(k)

Fig.10 Flow structures of cases with different blade profiles at ψ=0°. (a) NACA0009; (b) NACA0012; (c) NACA0015; (d) NACA0018; (e) NACA0022; (f) NACA2415; (g) NACA4415; (h) NACA6415; (i) Inverse NACA2415; (j) Inverse NACA4415; (k) Inverse NACA6415.

Then, four profiles, including NACA0015, 0022, 6415 and inverse NACA6415, are selected to study the blade profile effect. The performance of the cycloidal rotor and single blade for cases with various blade profiles are plotted in figure 11. It is evident that NACA6415 produces the highest lift and propulsive force coefficients, which nearly occurs at every position in a rotating cycle. For the distribution of the lift coefficient, the main difference appears from ψ=0° to 145°, while it ranges from ψ=0° to 100° for the propulsive force coefficient. However, the change of forces for NACA6415 is more evident than other profiles. According to the force distribution of the single blade, it concludes that blade B is the main contributor to the vertical force production because of the high vertical force generated at ψ=180°-360°, while both blade A and B take the responsibility to the generation of the propulsive force. To clarify the mechanism of flow-induced performance change, the difference of the lift and propulsion force coefficients difference at ψ=46° for cases with various blade cambers are clarified in detail in the following part.

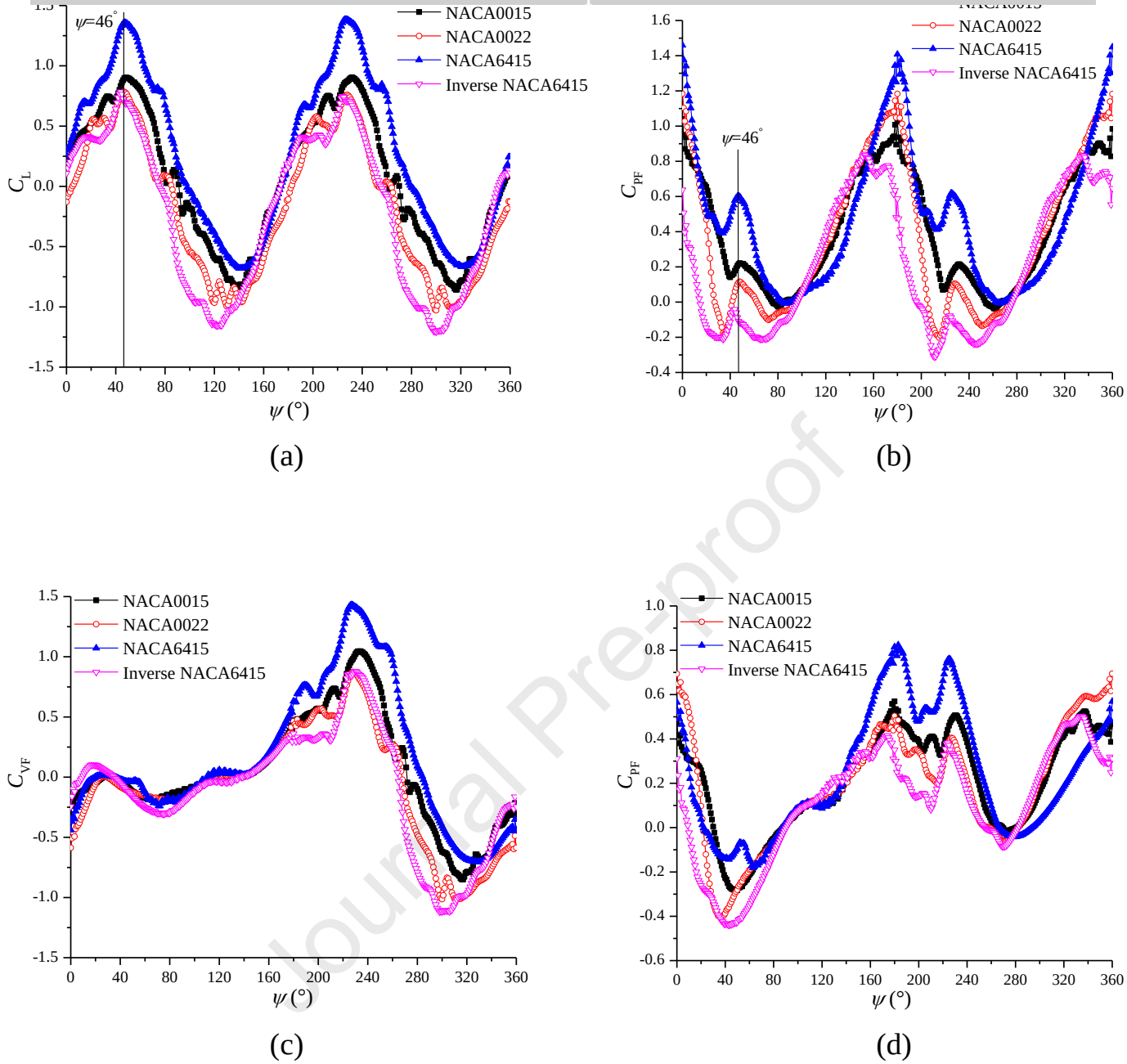

Fig.11 Performance of the cycloidal rotor and single blade. (a) Lift coefficient of the rotating system; (b) Propulsive force coefficient of the rotating system; (c) Vertical force coefficient of the single blade; (d) Propulsive force coefficient of the single blade.

The general flow structures, pressure coefficients and near-wall flow of two blades at ψ=46°, are displayed in figure 12. At this position, the main flow separation occurs on blade A and it leads to the intensive vortex shedding, which interacts with the leading edge of blade B directly. With the increase of the blade thickness of symmetrical profiles, the vortical flow is more evident, which consumes more power for the rotating system. In addition, the flow separation on both sides of blade A in figure 12c is violent and the wake shedding from blade B is approaching to itself. However, when it comes to the inverse asymmetrical blade, the flow separation on blade A and wakes of blade B become mild, which reduces the power consumption

significantly. By the comparison of the near-wall flow, it seems that it is more complicated on blade A surface. For an example, as the symmetrical blade thickness increases, the attached vortex occupies the large part of the pressure side and the flow separation vortex near the trailing edge of the suction side has already shed into the wake. Then, the massive flow separation emerges on both sides of NACA6415, leading to the large pressure fluctuation, especially on the pressure side. However, as the blade is in inverse mode, the flow is quite smooth, which is shown in figure 12j. In figure 11c, it is observed that the vertical force produced by different profiles at ψ=46° has almost no difference, because of the relatively small blade loading in figure 12e and the component of the lift balanced by the drag component in vertical direction. When it comes to the blade B, it is found that the pressure difference is much larger, although the near-wall flow for NACA0015, 0022 and 6415 are quite similar. It shows that the flow separation only appears near the trailing edge of the suction side, which is more obvious for NACA6415. It is very interesting that a separation bubble occurs on the leading edge of the suction side for inverse NACA 6415. Before the location of x/c=0.3, the pressure difference of inverse NACA6415 is extremely large, but it decreases quickly. The resultant upward lift of NACA6415 creates the large vertical force due to the large blade loading in figure 12f, providing the large lift to the cycloidal rotor. Thus, it concludes that blade B is dominate for the lift production of the rotating system.

The mean propulsive force coefficients for various profiles are also different at this azimuthal angle. The propulsive force distribution of single blade in figure 11d indicates that both two blades are responsible for that, but blade B is the main contributor. For a specific instance, for NACA6415, the upward lift towards the right side of blade A produces the negative propulsive force, but the magnitude is small due to the relatively small blade loading. The large pressure difference of blade B can result in the generation of large positive propulsive force. As a result, the sum of the propulsive force from two blades makes the positive propulsive force with large magnitude, as shown in figure 11b.

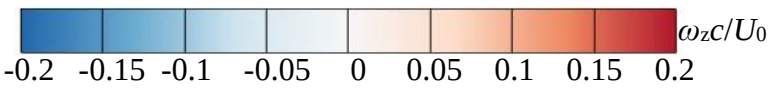

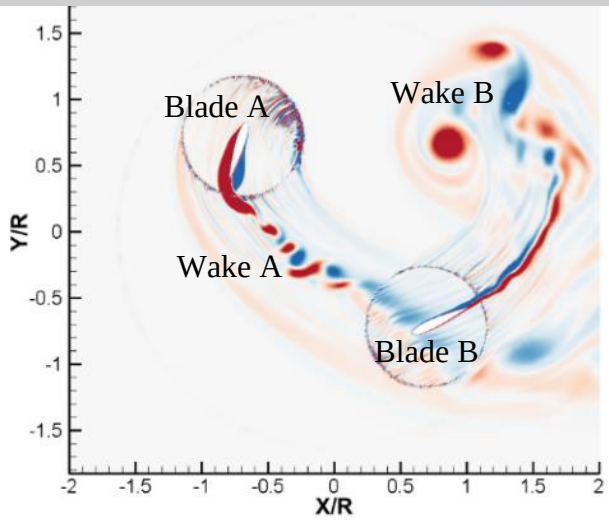

(a)

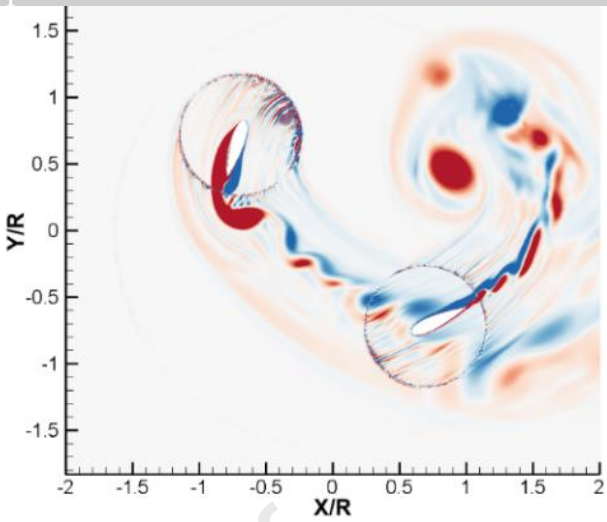

(b)

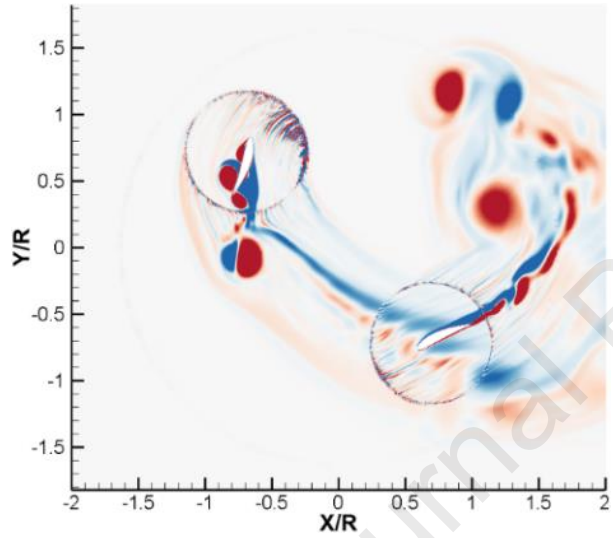

(c)

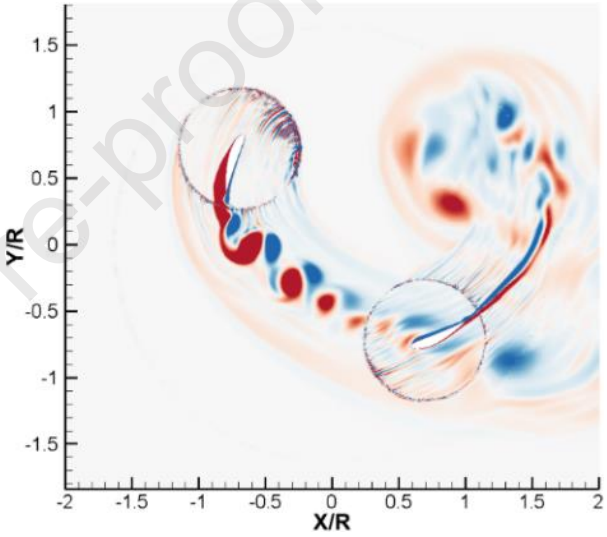

(d)

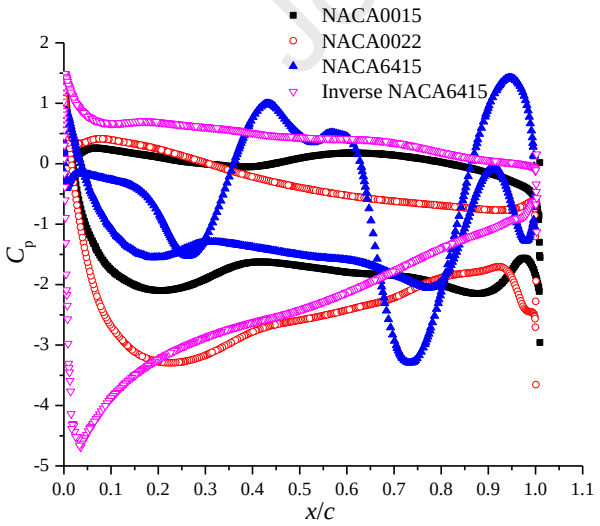

(e)

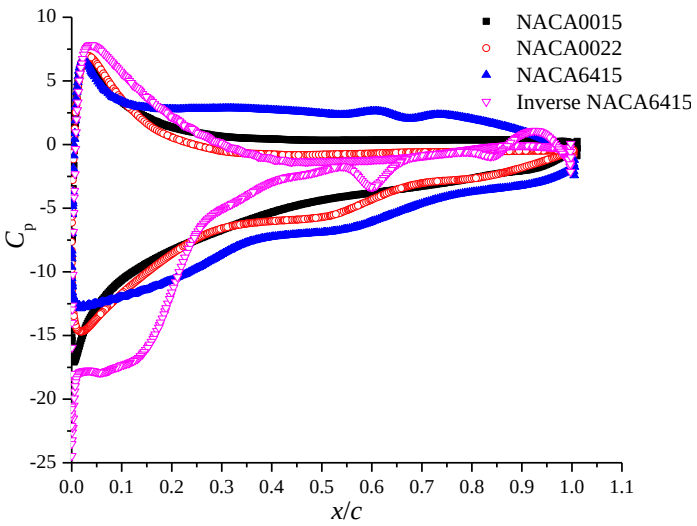

(f)

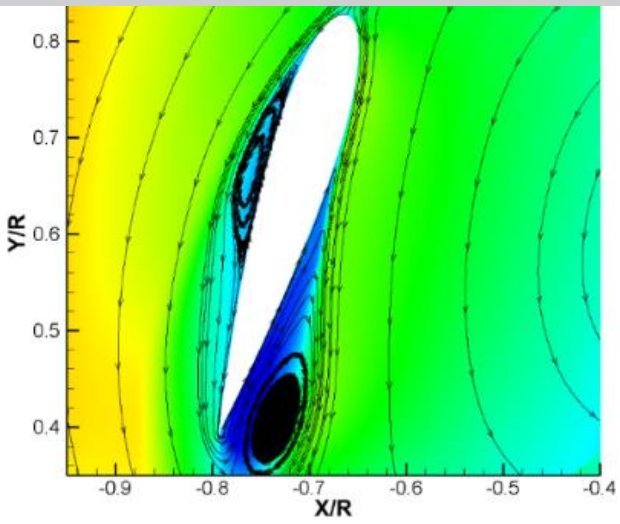

(g)

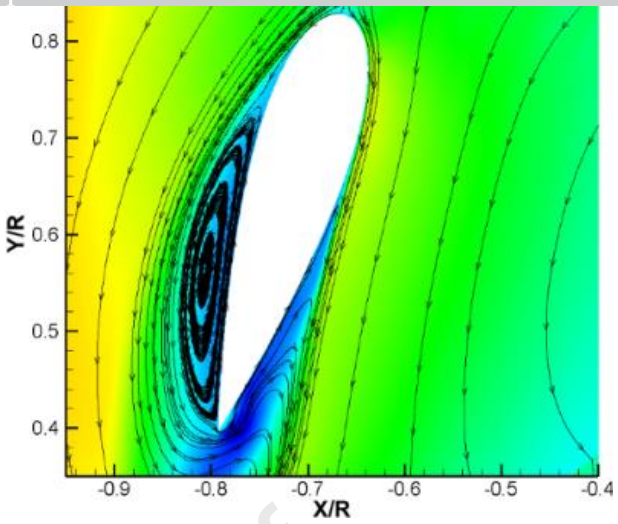

(h)

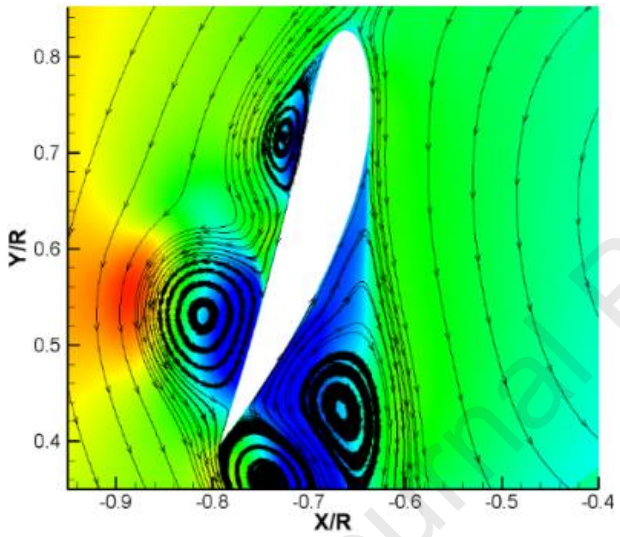

(i)

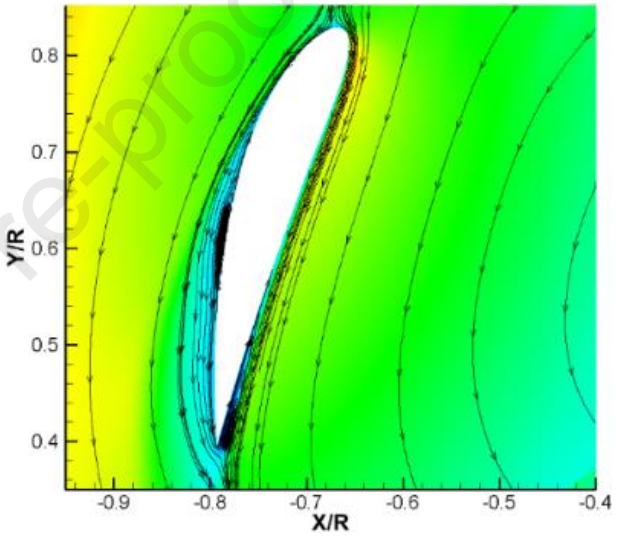

(j)

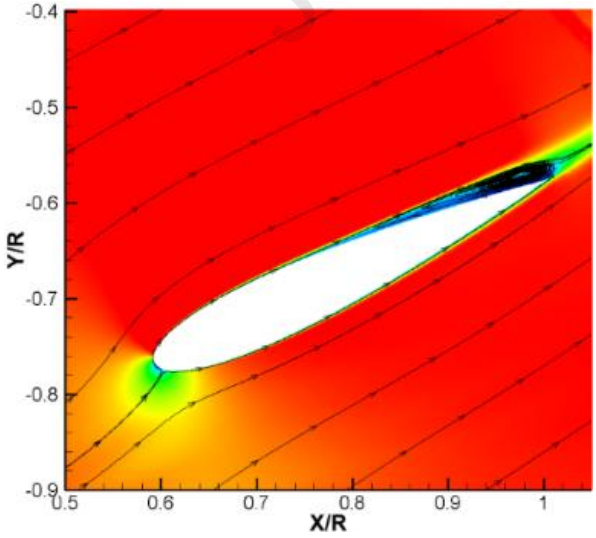

(k)

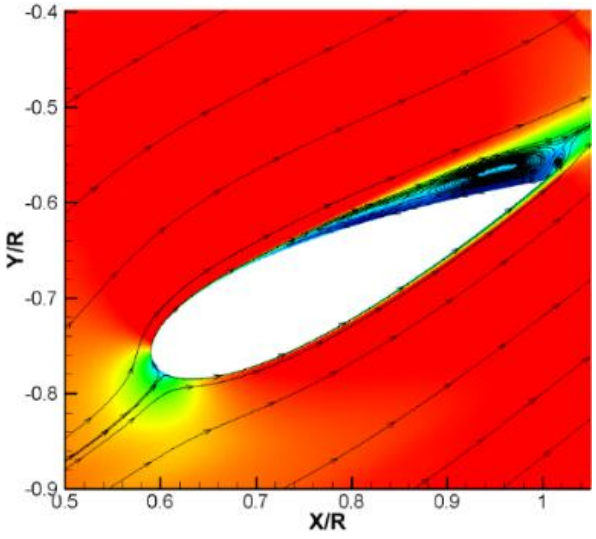

(l)

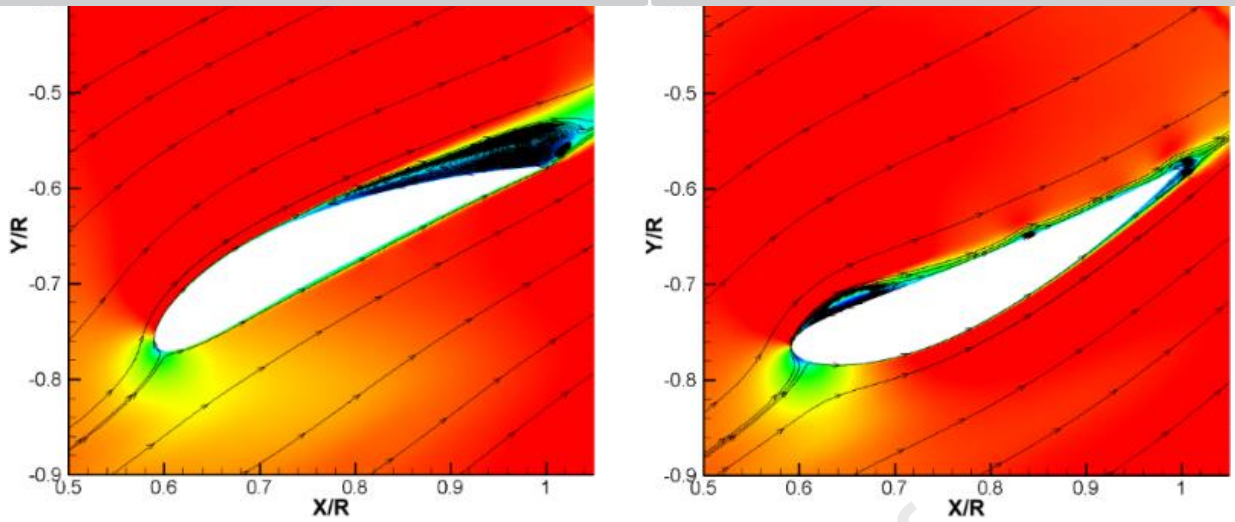

(m) (n)

Fig.12 Flow structures and pressure distributions of cases with various blade profiles at ψ=46°. (a), (g) and (k) NACA0015; (b), (h) and (l) NACA0022; (c), (i) and (m) NACA6415; (d), (j) and (n) NACA6415; (e) Pressure coefficient of blade A; (f) Pressure coefficient of blade B.

4.3 Effect of the advance coefficient

As an important parameter, shown in figure 13, the advance coefficient λ has great impact on the global performance and flow fields of the cycloidal propeller. With a constant value of λ, the profile of NACA6415 produces the largest lift, propulsive force and power coefficients. With the increase of λ by decreasing the rotating speed, the lift coefficient decreases for a specific profile, but it decreases firstly and then increases for NACA0022, inverse NACA4415 and 6415. The propulsive force coefficient decreases significantly with the increase of λ for all profiles, as well as the power coefficient. Then, regarding to the propulsive-force-based efficiency, it is observed that the symmetrical profiles operate in a wide range of high efficiency, but it becomes worse with the increase of the blade thickness. In addition, when λ is smaller than 0.5, the inverse NACA2415 achieves the best performance, but it decreases dramatically at high λ because of the relatively low propulsive force and high power. Moreover, although NACA6415 can generate the high propulsive force coefficient at various λ, but the efficiency is relatively low due to the high level of the power consumption. Furthermore, the efficiency of NACA0022, inverse NACA4415 and 6415 is negative as λ is larger than 0.625. Considering the stability of the working condition with high efficiency, the symmetrical profiles, including NACA0012 and 0015, are recommended for a better design of the cycloidal rotor.

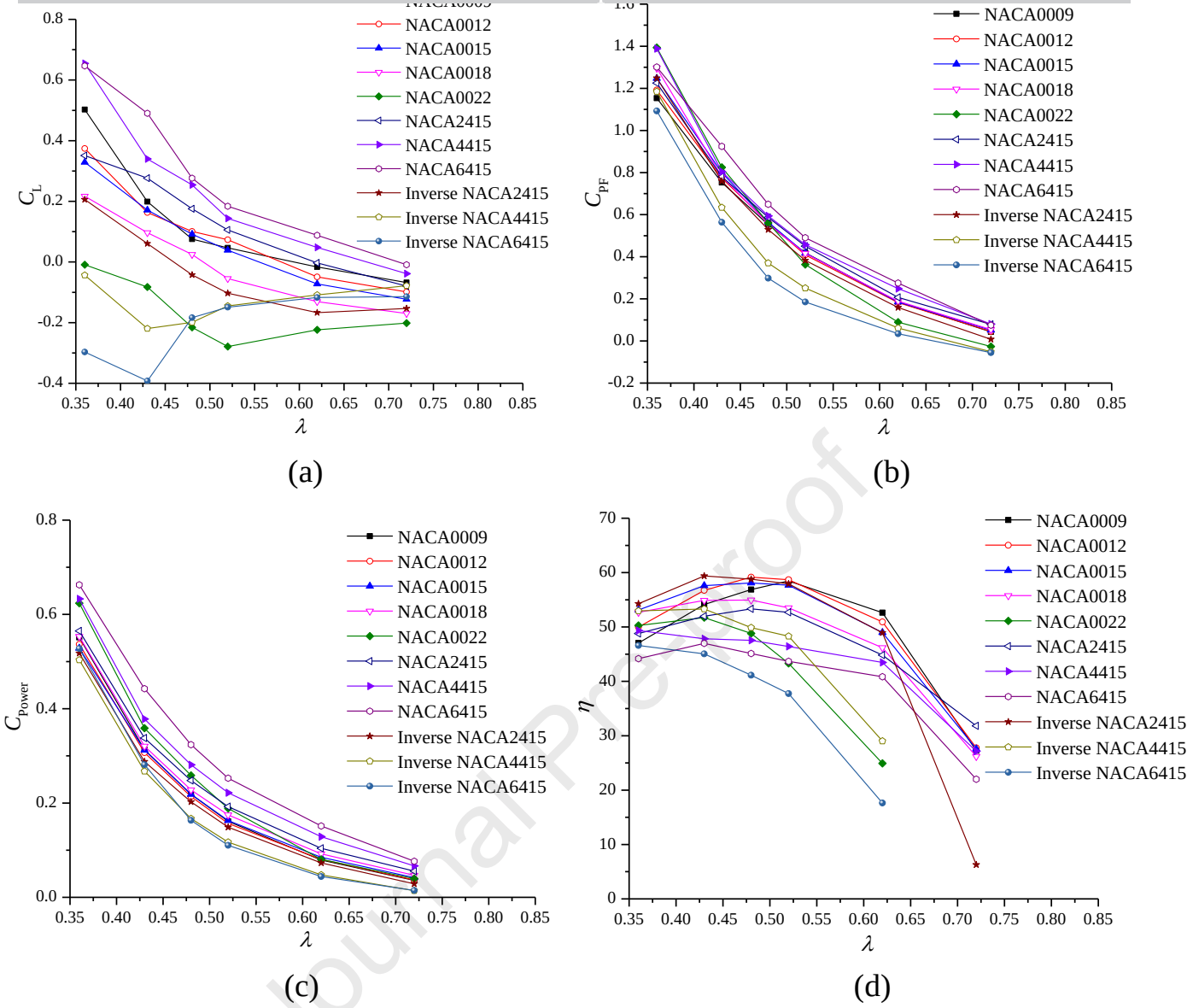

Fig.13 Time-averaged performance of the cycloidal rotor with different blade cambers at various λ. (a) Lift coefficient; (b) Propulsive force coefficient; (c) Power coefficient; (d) Efficiency.

By increasing the rotating speed, the advance coefficient λ decreases, which results in the significant change of the performance and flow structures. In figure 13, the lift, propulsive force and power coefficients decrease with the increase of λ. Therefore, two values of λ=0.43 and 0.72, representing the low and high advance coefficient, are employed in this work. The objective is NACA6415 profile because it can produce the highest force and power coefficients. The performance of the cycloidal rotor and single blade in a revolution are plotted in figure 14 to illustrate the force difference at two λ. In figure 14a, except the locations from ψ=110° to 180°, the lift coefficient is always much larger at low λ. Simultaneously, the propulsive force coefficient is also much larger at low λ at nearly every position of a rotating cycle. Then, for a single blade, at two regions of ψ=0°-30° and 290°-360°, the vertical

force coefficient at high λ is larger, but the propulsive force coefficient is always larger at low λ in a revolution. As a result, an azimuthal angle ψ=50° is selected to explain the performance difference induced by the internal flow structures at two λ.

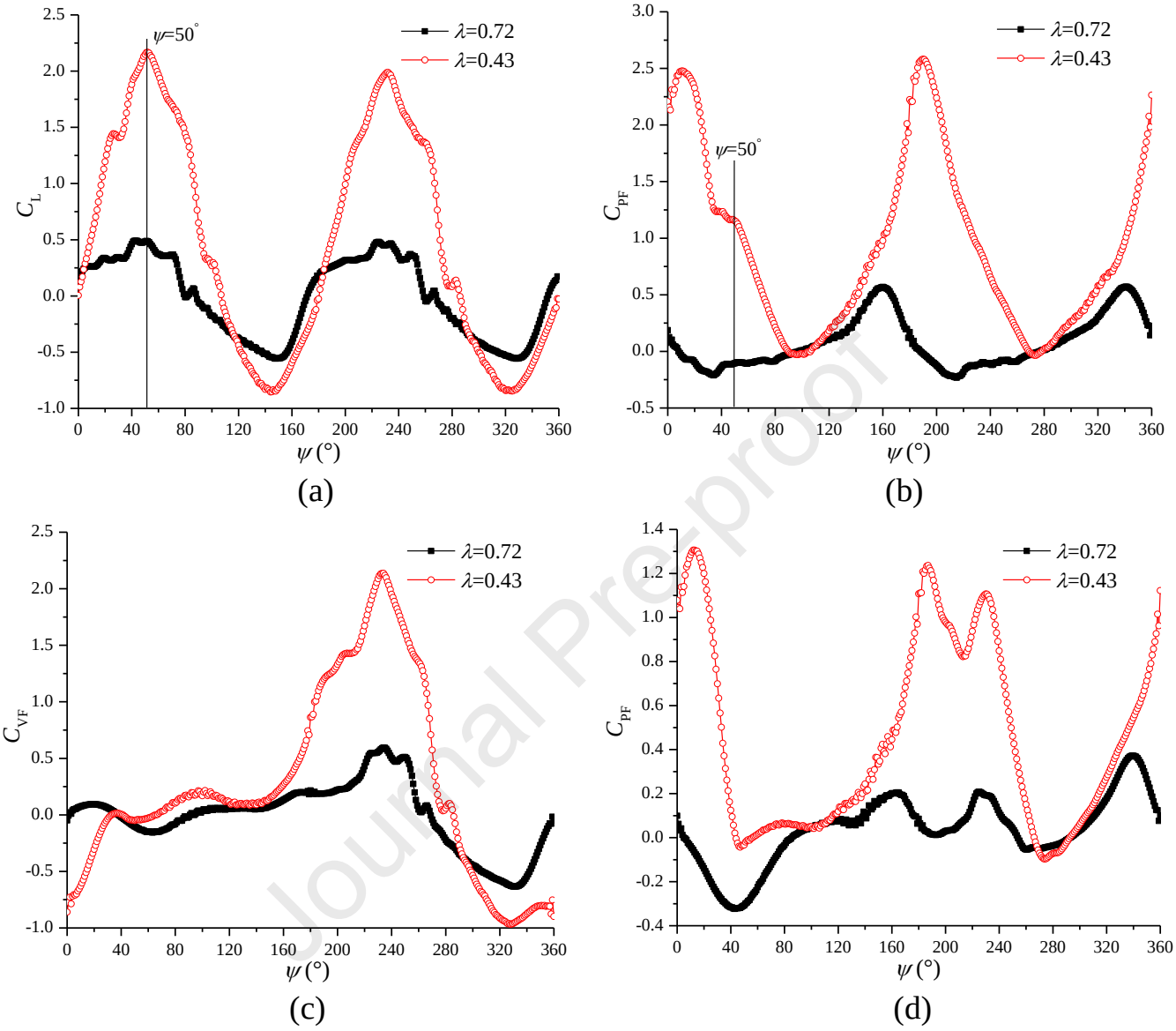

Fig.14 Performance of the cycloidal rotor and single blade at two advance coefficients. (a) Lift coefficient of the rotating system; (b) Propulsive force coefficient of the rotating system; (c) Vertical force coefficient of the single blade; (d) Propulsive force coefficient of the single blade.

In figure 15, to clarify the force coefficient difference, the flow structures and pressure distributions of two blades are displayed at ψ=50°. Evidently, at two λ, the wakes shedding from two blades are totally different. The wake A at low λ has already interacted with blade B, which is not clear at high λ. Additionally, the flow separation on both two sides of blade A is more intensive at low λ, which is responsible for the large value of the power coefficient. As λ decreases, it is observed that the stagnation point of blade A moves from left side of the leading edge to the right side, leading to the completely different boundary layer flows. For example, at

high λ, the size of vortex on the pressure side is relatively small and the trailing edge separation vortex on the suction side has large size, which is opposite at low λ. As a consequence, the pressure distributions at two λ are totally different, which is shown in figure 15c. At λ=0.72, the lift is downward towards the right side, causing the production of the negative propulsive force, but the magnitude is larger due to the components of lift and drag in the same direction. However, the propulsive force is nearly equal to zero at low λ, for the reason that the component of the lift is balanced by the drag component in the horizontal direction. Simultaneously, although the vertical force is the sum of components of lift and drag, it still has the small value due to the small blade loading at λ=0.43. Furthermore, on blade B, the flow separation only appears on the trailing edge of the suction side, which is stronger at low λ. It believes that the location of the stagnation point makes the contribution to the size of the trailing-edge separation vortex. At low λ, the pressure difference is much larger than that at high λ, which is responsible for the generation of the large positive vertical force and propulsive force. Therefore, the lift and propulsive force of the cycloidal rotor have the large values at low λ. Although blade B is the main contributor to the difference of the lift and propulsive force, blade A more or less makes the contribution to the propulsive force difference at two λ. In addition, the influence of the advance coefficient is more obvious than the Reynolds number effect due to the change of the rotating speed only, leading to the modification of the stagnation point location significantly, further altering the boundary layer flow, as shown in figure 16.

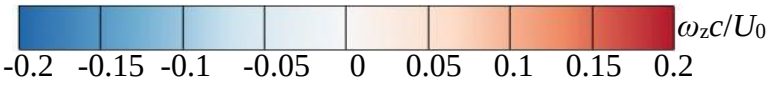

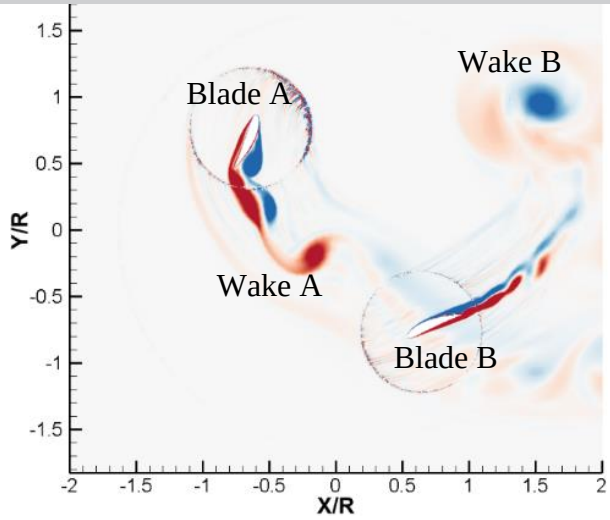

(a)

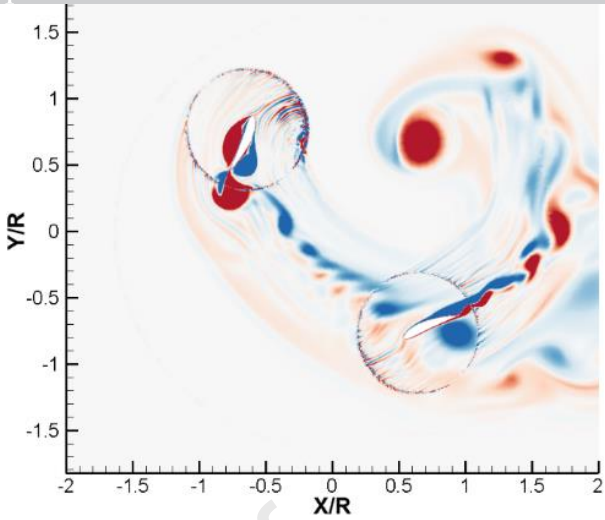

(b)

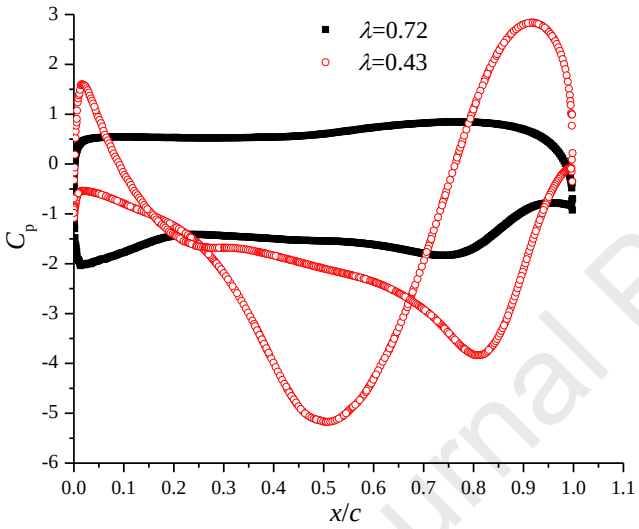

(c)

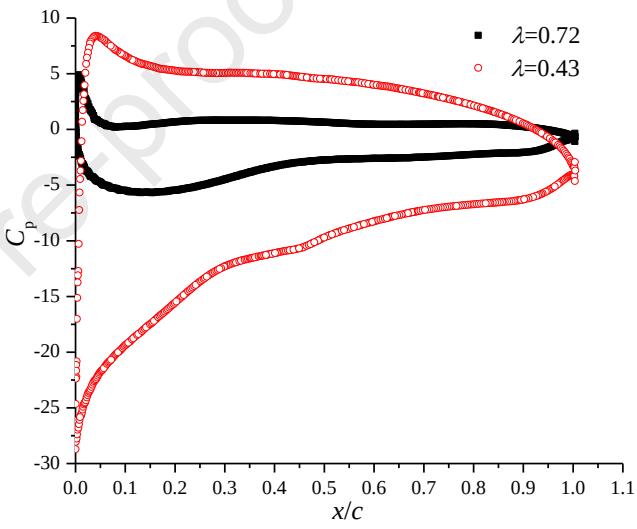

(d)

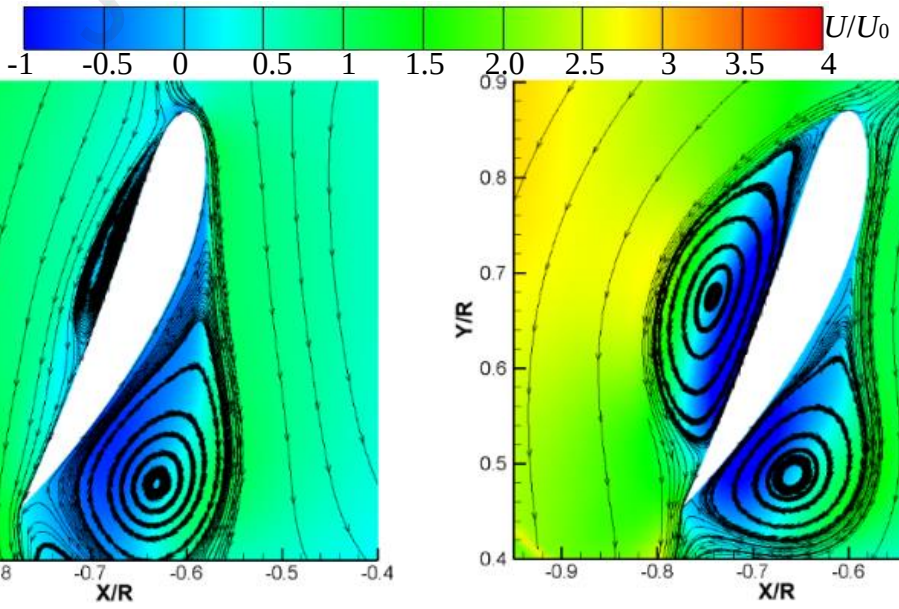

(e)

(f)

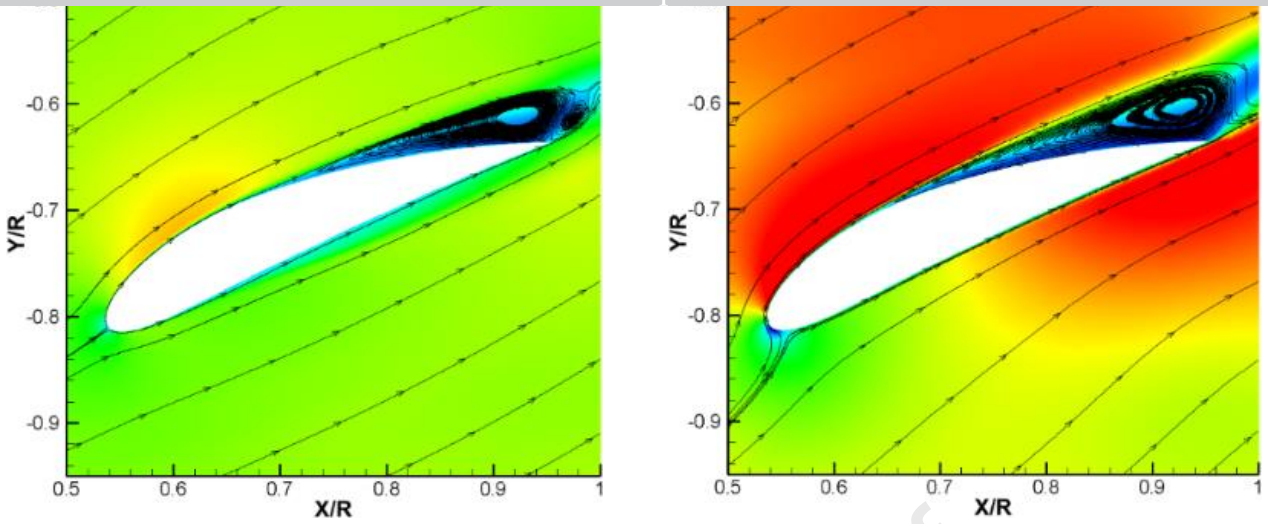

(g) (h)

Fig.15 Flow structures and pressure distributions of two blades at two λ at ψ=50°. (a), (e) and (g) λ=0.72; (b), (f) and (h) λ=0.43; (c) Pressure coefficient of blade A; (d) Pressure coefficient of blade B.

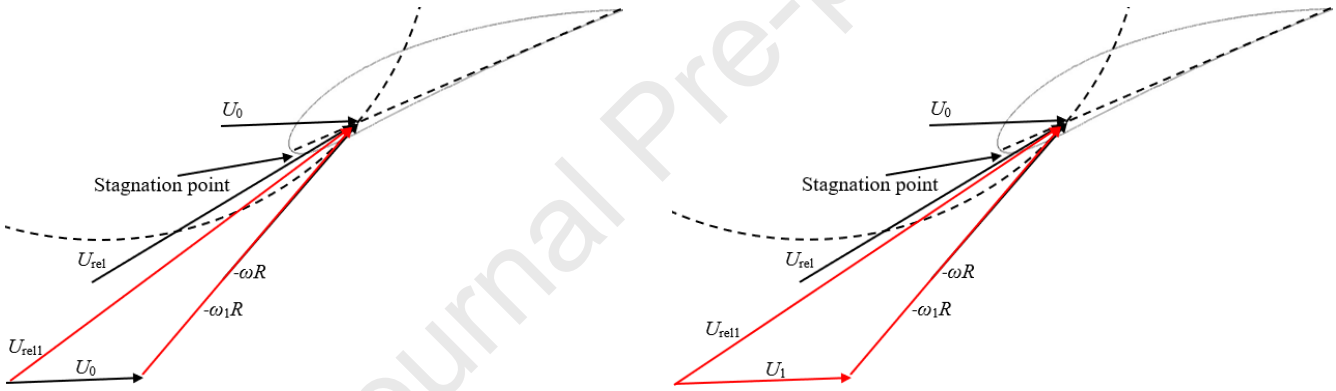

(a) (b)

Fig.16 Influence of λ and *Re* on the stagnation points. (a) λ effect; (b) *Re* effect.

5. Conclusions and future work

Two important parameters of a 2-bladed cycloidal rotor, including the pitch-pivot-point and blade camber, are investigated in this work, with special emphasis on the analysis of the performance and internal unsteady vortical flows under different working conditions. This work was performed with the aid of the SST $\gamma - \overline{Re}_{\theta t}$ transition model, together with the sliding mesh controlling the movement of the blades. In addition, for a specific blade profile, the influence of the advance coefficient is also studied. The main conclusions are made as follows:

(1) The present computations can obtain the good results compared with the previous numerical simulation and experimental measurements, in terms of the instantaneous performance curves and internal flow structures. The vortical flow

inside the cycloidal rotor is extremely complex, including the multiple blade-wake and wake-wake interactions at different azimuthal angles.

(2) The case with the pitch-pivot-point of x/c=0.25 obtains the best performance. When the pitching point moves towards the blade middle chord, though the propulsive force coefficient increases, the efficiency of the cycloidal rotor becomes worse because of the higher power that is consumed, which is ascribed to the massive flow separation and complicated vortical flows. Simultaneously, the lift coefficient increases and the flow separation on the blade surface occurs earlier as the pitch-pivot-point is closer to the leading edge. In the wake region, the velocity deficit concentrates in the windward side for the case with x/c=0.10 while it mainly appears in the centreline for the case with x/c=0.50.

(3) The symmetrical blade profiles, including NACA0012 and NACA0015, produce a best performance in achieving the efficiency, due to the relatively moderate propulsive force and power. In contrary, the asymmetrical profile, such as NACA6415, achieves the worst performance, due to the high consumption of the power. In addition, the inverse NACA2415 has a high potential to be optimized because it has a high efficiency at high *Re*. The large variation of the velocity profile in the wake region emerges in the windward side for NACA6415, but it both appears in the windward side and centerline for NACA0022, which can be explained by the disordered flow structures inside the propeller.

(4) Changing the rotating speed can significantly modify the stagnation point, leading to the totally different boundary layer flows at different λ. Normally, the difference of the lift coefficient depends on blade B, while both two blades should take the responsibility to the difference of the propulsive force of the cycloidal rotor. Generally, the performance difference of the cycloidal rotor should consider the performance, pressure difference, near-wall flow structure and forces (lift and drag) of each blade.

The present work only considers the rotor with 2 blades, it does not know if the pitching kinematic, chord-to-radius ratio, blade camber, pitch-pivot-point and other parameters are appropriate when the blade number increases. Additionally, the influence of the three-dimensional effect and aspect ratio on the performance, internal vortical flows, dynamic stall and turbulent wakes are still unknown. In the future, some advanced turbulence models considering the transition effect, such as Improved Delayed Detached Eddy Simulation (IDDES) $\gamma - \overline{Re}_{\theta t}$ transition model or Large Eddy Simulation (LES), are used due to the high resolution of the flow structure.

Acknowledgement

This work is financially supported by Senior Talent Grant Project of Jiangsu University (5501440012).

Nomenclature

c	Blade chord (m)
R	Rotor radius (m)
U_0	Freestream velocity (m/s)
n	Rotating speed (r/min)
θ	Instantaneous pitch angle (°)
θ_0	Mean pitch angle (°)
θ_{amp}	Pitch amplitude (°)
λ	Advance coefficient
Re	Reynolds number
C_L	Lift coefficient
C_{VF}	Vertical force coefficient
C_{PF}	Propulsive force coefficient
C_{Power}	Power coefficient
η	Propulsive force efficiency
ψ	Azimuthal angle (°)
γ	Intermittency
$\overline{Re_{\theta t}}$	Transition momentum thickness Reynolds number
$y+$	Dimensionless wall distance
u_τ	Wall friction velocity (m/s)
C_p	Pressure coefficient
p	Local pressure (Pa)
ω_z	Spanwise vorticity (1/s)
ν	Kinematic viscosity (m^2/s)

References

[1] Lind, A. H., Jarugumilli, T., Benedict, M., Lakshminarayan, V. K., Jones, A. R., & Chopra, I. (2014). Flow field studies on a micro-air-vehicle-scale cycloidal rotor in forward flight. *Experiments in Fluids*, *55*(12), 1-17.

[2] Tian, W., Bodling, A., Liu, H., Wu, J. C., He, G., & Hu, H. (2016). An experimental study of the effects of pitch-pivot-point location on the propulsion performance of a pitching airfoil. *Journal of Fluids and Structures*, *60*, 130-142.

[3] Xisto, C. M., Páscoa, J. C., & Trancossi, M. (2016). Geometrical parameters influencing the aerodynamic efficiency of a small-scale self-pitch high-solidity VAWT. *Journal of Solar Energy Engineering*, *138*(3), 031006.

[4] Benedict, M., Jarugumilli, T., Lakshminarayan, V., & Chopra, I. (2014). Effect of flow curvature on forward flight performance of a micro-air-vehicle-scale cycloidal-rotor. *AIAA Journal*, *52*(6), 1159-1169.

[5] Benedict, M., Jarugumilli, T., & Chopra, I. (2013). Effect of rotor geometry and blade kinematics on cycloidal rotor hover performance. *Journal of Aircraft*, *50*(5), 1340-1352.

[6] Jarugumilli, T., Benedict, M., & Chopra, I. (2011). Experimental optimization and performance analysis of a MAV scale cycloidal rotor. In *49th AIAA Aerospace Sciences Meeting including the New Horizons Forum and Aerospace Exposition*, 821.

[7] Zhang, H., Hu, Y., Wang, G., Fan, Z., & Wang, Y. (2016). An investigation into the effect of airfoil camber on the aerodynamics of MAV scale cycloidal propeller under hovering status. In *34th AIAA Applied Aerodynamics Conference*, 4169.

[8] Tang, J., Hu, Y., Song, B., & Yang, H. (2017). Unsteady aerodynamic optimization of airfoil for cycloidal propellers based on surrogate model. *Journal of Aircraft*, *54*(4), 1241-1256.

[9] Zhang, Y., Zhu, X., Song, X., Cai, C., Zhou, T., Kamada, Y., Maeda, T., Wang, Y., & Guo, Z. (2022). Effect of the bionic blade on the flow field of a straight-bladed vertical axis wind turbine. *Energy*, *258*, 124834.

[10] Zhu, X., Guo, Z., Zhang, Y., Song, X., Cai, C., Kamada, Y., & Maeda, T. (2022). Numerical study of aerodynamic characteristics on a straight-bladed vertical axis wind turbine with bionic blades. *Energy*, *239*, 122453.

[11] Ibrahim, A. A., Elbaz, A. M., Melani, P. F., Mohamed, O. S., & Bianchini, A. (2022). Power augmentation of Darrieus wind turbine blades using trapped vortex cavity. *Journal of Wind Engineering and Industrial Aerodynamics*, *223*, 104949.

[12] Abdolahifar, A., & Karimian, S. M. H. (2022). A comprehensive three-dimensional study on Darrieus vertical axis wind turbine with slotted blade to reduce flow separation. *Energy*, *248*, 123632.

[13] ul Hassan, S. S., Javaid, M. T., Rauf, U., Nasir, S., Shahzad, A., & Salamat, S. (2023). Systematic investigation of power enhancement of Vertical Axis Wind Turbines using bio-inspired leading edge tubercles. *Energy*, *270*, 126978.

[14] Shi, L., Bayeul-Lainé, A. C., & Coutier-Delgosha, O. (2022). Analysis of flow-induced performance change of cycloidal rotors: Influence of pitching kinematic and chord-to-radius ratio. *Ocean Engineering*, *263*, 112382.

[15] Shi, L., Bayeul-Lainé, A. C., & Coutier-Delgosha, O. (2022). Numerical investigations on unsteady vortical flows and separation-induced transition over a cycloidal rotor at low Reynolds number. *Energy Conversion and Management*, *266*, 115812.

[16] Rezaeiha, A., Montazeri, H., & Blocken, B. (2019). On the accuracy of turbulence models for CFD simulations of vertical axis wind turbines. *Energy*, *180*, 838-857.

[17] Jarugumilli, T. (2013). An experimental investigation of a micro air vehicle-scale cycloidal rotor in forward flight. Doctoral dissertation, University of Maryland, College Park.

[18] Li, X., Feng, L. H., & Li, Z. Y. (2019). Flow mechanism for the effect of pivot point on the aerodynamic characteristics of a pitching airfoil and its manipulation. *Physics of Fluids*, *31*(8), 087108.

Highlights

- The SST γ-$Re_{\theta t}$ transition model coupled with the sliding mesh method are used for a 2-bladed cycloidal propeller
- Effects of the pitch-pivot-point and blade camber are discussed
- Influence of the Reynolds number and advance coefficient are clarified